F-actin patches associated with glutamatergic synapses control positioning of dendritic lysosomes

Bas van Bommel[1*], Anja Konietzny[1*], Oliver Kobler[2], Julia Bär[1], Marina Mikhaylova[1#]

[1]DFG Emmy Noether Group 'Neuronal Protein Transport', Center for Molecular Neurobiology, ZMNH, University Medical Center Hamburg-Eppendorf, 20251 Hamburg, Germany

[2]Combinatorial Neuroimaging Core Facility (CNI), Leibniz Institute for Neurobiology, 39118 Magdeburg, Germany

* these authors contributed equally to this work

corresponding author: marina.mikhaylova@zmnh.uni-hamburg.de

Running title: Dendritic F-actin traps lysosomes

Key words: lysosome, shaft synapse, F-actin, myosin, microtubule

Abstract

Organelle positioning within neurites is required for proper neuronal function. In dendrites with their complex cytoskeletal organization, transport of organelles is guided by local specializations of the microtubule and actin cytoskeleton, and by coordinated activity of different motor proteins. Here, we focus on the actin cytoskeleton in the dendritic shaft and describe dense structures consisting of longitudinal and branched actin filaments. These actin patches are devoid of microtubules and are frequently located at the base of spines, or form an actin mesh around excitatory shaft synapses. Using lysosomes as an example, we demonstrate that the presence of actin patches has a strong impact on dendritic organelle transport, as lysosomes frequently stall at these locations. We provide mechanistic insights on this pausing behavior, demonstrating that actin patches form a physical barrier for kinesin-driven cargo. In addition, we identify myosin Va as an active tether which mediates long-term stalling. This correlation between the presence of actin meshes and halting of organelles could be a generalized principle by which synapses control organelle trafficking.

Introduction

The ability of neurons to convey and store information is based on their intricate and complex architecture, which allows a multitude of synaptic cell-to-cell contacts. The most-studied and most prevalent type of synaptic contacts are excitatory spine synapses, which are located on small dendritic protrusions called spines. The actin cytoskeleton, together with scaffolding molecules at the post-synaptic density (PSD), establishes the spine architecture and enables tuning of synaptic strength. Actin in the spine has been the focus of extensive research efforts, and various functions of filamentous actin (F-actin) in dendritic spines have been described in detail (Bär et al, 2016; Hlushchenko et al, 2016; Kim et al, 2015; Korobova & Svitkina, 2010; Matus, 2000; Mikhaylova et al, 2018; Svitkina et al, 2010). Spinous F-actin is classified by filament type (branched or longitudinal) and functionally divided into a stable and dynamic pool. Actin dynamics are instrumental for activity-dependent structural plasticity of dendritic spines (Bosch et al, 2014; Kim et al, 2015; Matsuzaki et al, 2004; Mikhaylova et al, 2018; Racz & Weinberg, 2013). In addition to synapses located on spines there is a smaller fraction of glutamatergic synapses formed directly on the dendritic shaft, but their contribution to neuronal function is investigated to a lesser extent (Bourne & Harris, 2011; Reilly et al, 2011).

Plasticity and stability of synaptic contacts relies on several factors, including transport and delivery of proteins and mRNA from the soma, local dendritic protein synthesis, surface diffusion of membrane proteins, recycling of synaptic proteins via the dendritic secretory trafficking system, as well as controlled disposal of ‘aged’ molecules mediated by lysosomes, autophagosomes, and the proteasomal system (Bowen et al, 2017; Goo et al, 2017; Penn *et al*, 2017; Hanus & Schuman, 2013; Mikhaylova et al, 2016; Nirschl et al, 2017; Seipold et al, 2018). Various secretory trafficking organelles are present along dendrites and help to regulate the protein pool required for potentiation and stabilization of specific synaptic contacts (van Bommel & Mikhaylova, 2016).

Recently we and others could demonstrate that synaptic activity restrains lateral movement of ERGIC (ER to Golgi intermediate compartment), dendritic Golgi satellites, and retromer, bringing them into close spatial proximity for confined processing of secretory cargo (Hanus et al, 2014; Mikhaylova et al, 2016). Also trafficking of lysosomes is influenced by synaptic activation. Goo and colleagues showed that lysosomes move bidirectionally in dendrites and can be stalled at the base of individual spines in response to local synaptic stimulation (Goo et al, 2017). In addition, neuronal activity can trigger the Ca^{2+}-dependent fusion of lysosomes with the dendritic plasma membrane, resulting in the release of lysosomal proteases, including cathepsin

B. This leads to the activation of matrix metalloproteinase 9, which is instrumental for the remodelling of the extracellular matrix that in turn allows spine growth and long-term potentiation (Padamsey et al, 2017).

How could such precise organelle targeting and localization be achieved? Organelle transport critically relies on the microtubule (MT) and F-actin cytoskeleton. MTs serve as tracks for long-range active transport driven by kinesin (plus-end directed) and dynein (minus-end directed) motors, whereas actin-based myosin motors regulate short-range transport and organelle tethering (Konietzny et al, 2017). Processive myosin V and VI are implicated in the transport of transmembrane proteins, such as ion channels, receptors and transporters, in and out of dendritic spines (Esteves da Silva et al, 2015; Kneussel & Wagner, 2013). Most intracellular cargoes are bound by multiple and different motors, which, in combination with the cytoskeletal architecture, define the transport characteristics of organelles (van Bergeijk et al, 2016). In a recent study, Janssen and colleagues showed that inducible recruitment of constitutively active kinesin-1 (KIF5B) to immobile somatic peroxisomes is sufficient to drive transport into the axon (Janssen et al, 2017). Additional recruitment of constitutively active myosin V to the same organelle rapidly anchored them at the actin-rich axon initial segment, illustrating how combinational motor activity can influence transport. Interestingly, myosin V-induced anchoring of peroxisomes was sometimes observed along the axon, in dendrites and in the soma, suggesting that it occurs whenever cargoes with active myosin V encounter actin-rich regions (Janssen et al, 2017). In addition to active anchoring mechanisms, the presence of dense cytoskeletal structures and other organelles can create physical obstacles for cargo trafficking (Katrukha et al, 2017). Moreover, dense patches of F-actin found at the base of some dendritic spines can form obstacles for microtubule growth, directing them into spines. Synaptic activity increases the amount of F-actin in spine-associated patches, which correlates with increased probability of microtubule entry (Schätzle et al, 2018).

In recent years, advanced microscopy techniques have led to the discovery of novel F-actin based structures in neurites. Perhaps the most striking and extensively studied is the periodic actin-spectrin lattice that covers the lengths of axons, dendrites and dendritic spine necks (Bär et al, 2016; D'Este et al, 2015; He et al, 2016; Xu et al, 2013). Furthermore, previously undescribed patches and bundles of F-actin have been observed along the lengths of dendrites, and were suggested to serve as outgrowth points for filopodia, although their function is so far unknown (Willig et al., 2014, Korobova and Svitkina, 2010).

Here, we have mapped the dendritic actin cytoskeleton of mature hippocampal neurons and found local enrichments of F-actin within the dendritic shaft and at the base of dendritic spines. These F-actin patches frequently co-localized with excitatory synapse markers and contain a mixture of linear and branched filaments. Additionally, we discovered that local actin enrichments act as a regulator of lysosome trafficking, as lysosomes frequently pause at these loci. We show that the F-actin mesh acts both as a passive, physical barrier, slowing down transport of vesicles driven by MT motors, and as an anchoring point for active stalling of vesicles via myosins. These findings indicate a critical role of F-actin within dendrites, orchestrating organelle transport and positioning near synaptic contacts.

Results

F-actin patches frequently colocalize with synaptic markers

The organization and functional relevance of the actin cytoskeleton in dendritic shafts of mature hippocampal neurons has not been investigated in much detail so far. To map the distribution of F-actin in dendrites, we initially performed immunostainings of DIV17 neurons with the F-actin dye phalloidin-Atto647N and for the dendritic microtubule marker MAP2. Confocal imaging suggested the presence of F-actin enrichments in dendritic shafts (Figure EV1A). To characterize the nanoscale organization of dendritic F-actin, we employed high resolution stimulated emission depletion (STED) imaging (Figure 1A; Figure EV1A). In addition to the periodic cortical F-actin lattice in dendritic shafts and spine necks, we clearly observed local enrichments of F-actin adjacent to the plasma membrane, sometimes localized at the base of dendritic spines (Figure 1A). To verify the dendritic origin of these patches, we transfected DIV16 hippocampal neurons with a plasmid encoding an anti-actin nanobody (hereafter referred to as chromobody) fused to eGFP and tagBFP as cell fill. Chromobodies and phalloidin-Atto647N labelled the same dendritic F-actin foci as evident from the confocal and STED images (Figure 1B). These F-actin patches develop with the maturation of primary cultured neurons, and were first detectable at approximately DIV6 (Figure EV1B). Their time of appearance coincided with synaptogenesis, and co-localization with the presynaptic marker bassoon indicated a spatial relationship with synapses (Figure EV1B). This close proximity to presynaptic sites extended to mature neurons (DIV 16) where the actin patches were also positive for bassoon (Figure 1C, Figure EV1C). The presence of bassoon suggests that a proportion of the dendritic actin patches are part of synaptic contacts.

Both excitatory glutamatergic synapses and inhibitory GABAergic synapses can be found on the dendritic shaft and are contacted by bassoon-positive presynapses (Richter et al, 1999). To distinguish between them, we performed a complementary staining with excitatory and inhibitory postsynaptic markers (homer1 and gephyrin, respectively / Figure 2A-C). Analysis indicated a high degree of co-localization of phalloidin-A647N-labelled actin patches with homer1 (65 %), but to a much lesser degree with gephyrin (12.5 % / Figure 2D). In DIV17-21 primary neurons, F-actin patches were present with an average frequency of 3.5 per 10 µm of dendritic shaft (Figure 2D). About 23 % of them were located at the base of dendritic spines (Figure 2E). Detailed analysis of 2D STED data showed that the patch size varied between 0.02 - 0.5 μm^2. Interestingly, patches within the dendritic shaft that contained homer1 were significantly larger than these without (Figure 2F). About one half of patches located at the base of dendritic spines contained a PSD but their size was not influenced by the presence of homer1 (Figure 2F).

Excitatory shaft synapses of principal neurons receive little attention compared to spine synapses, but they are clearly present in principal neurons of hippocampus and cortex (Bourne & Harris, 2011; Trachtenberg et al, 2002). 3D reconstructions of primary neurons transfected with mRuby2, the PSD marker FingRs-PSD95-GFP, and immuno-labelled for bassoon indicated the presence of both spine and shaft synapses in medial and distal dendrites of DIV17 neurons (Figure EV2A). In agreement with primary cultures, labelling of mature CA1 pyramidal neurons in hippocampal slice cultures with mRuby2 and FingRs-PSD95-GFP revealed the presence of excitatory shaft synapses on the apical dendrite and its branches (Figure EV2B, Movie 1). To address the functionality of axon terminals on these dendritic shafts we performed a synaptotagmin-1 antibody uptake assay (Ivanova et al, 2015). DIV17 hippocampal neurons were incubated with synaptotagmin-1 antibody for 30 minutes, then fixed and stained against F-actin and homer1. Confocal imaging showed that at basal synaptic activity, homer1 and F-actin positive puncta were frequently colocalized with synaptotagmin-1, indicating that actin-enriched areas oppose active presynaptic terminals (Figure 1G). The synaptotagmin-1 signal significantly decreased when the antibody was applied to tetrodotoxin (TTX) silenced cultures (Figure 2G, H). In addition, immunostaining of GFP filled neurons with antibodies against GluA1 and GluN1 indicated the presence of both α-amino-3-hydroxy-5-methyl-4-isoxazolepropionic acid (AMPA) and N-methyl-D-aspartate (NMDA) receptor subunits, indicating shaft synapses being active- rather than silent synapses (Figure 2I). Taken together, these results suggest that F-actin enrichments could be a common feature for synaptic contacts on spines and dendritic shafts, and

that the majority of the dendritic F-actin patches represent active excitatory shaft synapses containing both pre- and postsynaptic components.

Dendritic F-actin patches are dynamic and consist of branched and longitudinal filaments

In contrast to actin in spines, the structural composition of F-actin in dendritic patches is unknown (Bosch et al, 2014; Konietzny et al, 2017; Mikhaylova et al, 2018). In order to characterize the type of filaments present in dendritic actin patches, we performed pharmacological inhibitor experiments followed by immunostainings. Interestingly, spine-base associated actin patches were generally more sensitive to pharmacological perturbations than shaft-associated patches: upon depolymerization of F-actin induced by a 30 min treatment with latrunculin A (LatA; 5 µM), spine-base associated F-actin loci disappeared almost completely, while the number and intensity of shaft associated patches also decreased significantly, but to a much lower extent (Figure 3A, B, EV2 C, D). We next asked what types of filaments are present at dendritic actin patches. Inhibition of the main classes of F-actin nucleators, the Arp2/3 complex (CK666; 50 µM for 2 h) and formins (SMIFH2; 30 µM for 90 min), led to a strong reduction in the number of patches localized near the base of spines and a mild decrease in shaft associated patches (Figure 3B), while patch size and intensity remained largely unchanged (Figure EV3C, D). Moreover, both spine- and shaft-associated actin patches showed a correlation between the amount of F-actin and cortactin, a marker of branched and stable actin filaments (Figure 3A, C). In contrast to the axonal “hotspots” described by Ganguly et al., which originate from F-actin nucleation by stationary endosomes, disruption of endosomes by brefeldin A treatment (100 ng/ml) had no noticeable effect on the size and localization of dendritic actin patches, suggesting an endosome-independent nature of these structures (Ganguly et al. 2015 / Figure EV2E).

The fact that small F-actin puncta remained after LatA treatment could be an indication for a stable pool of actin filaments present in dendritic actin patches. To directly investigate the rate of actin turnover we transfected neurons with actin-RFP and performed fluorescence recovery after photobleaching (FRAP) measurements. The FRAP kinetics suggests that dendritic actin patches contain dynamic and stable actin pools, with similar dynamics to actin in spines (Figure 3D, E). In addition, time-lapse imaging of F-actin labeled by expression of chromobody revealed that dendritic actin patches are relatively stable, do not move and are persistent in their location over at least 60 min (Figure EV3A, B). In summary, dendritic F-actin patches appear to be stably localized over time, and similarly to spinous F-actin consist of both branched (Arp2/3-nucleated)

and linear (formin-nucleated) filaments. They have a relatively high turnover rate and contain a depolymerization-resistant, stable F-actin pool.

Dendritic F-actin patches are spatially segregated from the microtubule cytoskeleton and control positioning of dendritic lysosomes

We hypothesized that dendritic F-actin patches act as a regulator of organelle and vesicular trafficking. We therefore decided to take a detailed look at the spatial organization of F-actin and MTs in dendrites, using STED nanoscopy on DIV17 neurons stained with phalloidin-Atto647N and α-tubulin antibodies. Intriguingly, we found that MT bundles, while closely associated with the F-actin lattice close to the cell membrane, were clearly spatially separated from dendritic actin patches rather than passing through them (Figure 4A).

To address the question if dendritic actin patches influence organelle trafficking, we chose to look at lysosomes as a representative vesicular organelle, because they show very active, processive trafficking along dendrites, and recently more and more studies are emerging that highlight their significance in neuronal function (Cheng et al, 2018; Goo et al, 2017; Padamsey et al, 2017). First, we used 3-color STED to visualize the spatial relationship between F-actin, MTs and lysosomes, using antibodies against the lysosomal marker protein LAMP1. We found that LAMP1 puncta were distributed all over the dendrite, with some puncta fully embedded into the F-actin mesh, while others were located next to MTs or at the interface between the F-actin and MT bundles (Figure 4B). This indicates that lysosome transport and positioning relies on both the organization of the microtubule and actin cytoskeleton.

Next, we looked at the trafficking characteristics of lysosomes in live DIV17 neurons using the fluorescent dye LysoTracker or LAMP1-eGFP expression, both labeling acidified late endosomes and lysosomes. Here we use the term lysosomes collectively for LysoTracker or LAMP1-positive organelles. As we have shown previously that LatA treatment greatly reduces the number of dendritic actin patches (Figure 3A, B), we used the same strategy to investigate the effect of actin patches on lysosome trafficking. Using kymograph analyses we found that depolymerization of actin filaments with LatA clearly increased the mobile fraction of lysosomes as judged by various parameters: total time spent in a mobile state increased (Figure 5A-B; Figure S1; Movie 2) summed pausing time was reduced (Figure 5C) and pausing times were generally shorter (Figure 5D). Interestingly, directional net flux analysis indicated that LatA treatment had an effect on the directionality of trafficking (Figure 5E). On the other hand, the instant velocity and instant run length did not change (Figure 5F, G). However, a shortcoming of

LysoTracker is that it indiscriminately stains all cells in a culture. To exclude lysosomal contribution from unrelated cells in the kymograph analysis, we transfected hippocampal neurons with LAMP1-eGFP and repeated the same experiments at DIV16-17. Similarly, we found that LAMP1-eGFP vesicles became more mobile following actin depolymerization (Figure 5H-K) and the directional net flux was no longer biased towards anterograde trafficking (Figure 5L). Overall, LAMP1-labelled vesicles were slightly more mobile than LysoTracker stained organelles, which probably has to do with the broader spectrum of endolysosomal compartments labeled by LAMP1 (Cheng et al, 2018). Altogether, these data suggest a contribution of the dendritic F-actin cytoskeleton in directing trafficking of lysosomes.

To directly observe how the presence of actin patches influences lysosomal stalling in dendrites, we co-transfected LAMP1-eGFP and chromobody-tagRFP. Time lapse imaging followed by kymograph analysis revealed that lysosomes indeed frequently stop, reverse or anchor at F-actin-rich structures located within the dendrite or at the base of dendritic spines (Figure 6A; Movie 3). In order to obtain more quantitative information, we analyzed the average velocity of lysosomes (including stationary ones) inside or outside of actin-rich areas (Figure S2). The velocity of lysosomes in proximity to actin patches was significantly lower than in dendritic segments without accumulations of F-actin (Figure 6B). The significant effect was lost when the mask used to mark the F-actin enriched areas was randomly shifted (Figure 6B, Figure S2). This suggests that dense meshes of F-actin could create intracellular traps for organelles and either passively slow down MT-based trafficking or interrupt processive transport via active F-actin anchoring mechanisms.

Lysosomes are associated with different types of MT motors (kinesin-1, -2, dynein) (Farias et al, 2017; Pu et al, 2016), which makes it difficult to discriminate which motor might be primarily affected by the F-actin mesh, or if the presence of actin patches triggers competition between these motor proteins, a so called “tug-of-war”, resulting in stops and switches in transport directionality (Hancock, 2014). In order to be able to rule out tug-of-war effects, we decided to engineer a cargo that is only transported by one type of dendritic MT motor. For that we chose the plus-end directed motor KIF17 (kinesin-2), which is known to be involved in trafficking of dendritic secretory organelles and should therefore provide similar trafficking kinetics and pulling forces as for physiological cargo (Hanus et al, 2014). As a cargo we chose peroxisomes, small and relatively stationary organelles that are mostly present in the soma (Kapitein et al, 2010). Peroxisomes do not associate with myosin Va and VI motors as judged by immunoblotting and immunostaining of peroxisomes enriched from rat brain (Figure EV4A, B).

We artificially induced transport of peroxisomes by KIF17 via bicistronic expression of the peroxisomal targeting sequence of PEX3 fused to GFP, and a GFP nanobody (VHH_{GFP}) fused to constitutively active KIF17 (Figure EV4C). Live imaging of hippocampal neurons transfected with this construct revealed that a fraction of peroxisomes became mobile. The organelles were transported unidirectionally in axons and bidirectionally in dendrites, indicating that there is no additional minus-end directed motor (i.e. dynein) attached and there will indeed be no contribution of a "tug of war" to stalling and reversals of peroxisomes (Figure EV4C). Instant velocity and instant run length were the same in anterograde and retrograde directions, confirming the model of a single type of MT motor (Figure EV4D, E). We used this construct to measure the motility of peroxisomes in the proximity of F-actin patches as we did for lysosomes. We observed that mobile peroxisomes also frequently paused at F-actin patches as evident from the kymograph (Figure 6C, Movie 4). In contrast to lysosomes, we only analyzed peroxisomes showing at least one processive run during 3 min imaging periods to ensure that the cargo was associated with active KIF17. However, their average speeds did not differ between inside and outside of F-actin patches (Figure 6C, D; Movie 3). This is probably due to the high number of short stopping events that affect the average velocity relatively little (compare Figure 5 D, K control to Figure 6 H control). Furthermore, we induced actin depolymerization with LatA and compared various trafficking parameters as we did for lysosomes (Figure 6E-J). LatA treatment resulted in a decrease of the summed pausing time (72 % from control / Figure 6G), while the frequency distribution of the pause durations did not significantly differ from the distribution before the treatment (Figure 6H). This means that after LatA treatment, peroxisomes took fewer pauses, but the pause duration of stopped peroxisomes was unaltered. This could mean that actin patches are involved in triggering pauses, but not in long-term halting of this artificial cargo. Additionally, anterograde instant velocity and retrograde run length were reduced (Figure 6F, G). These results suggest that, similar to lysosomes, kinesin-transported peroxisomes can interact with the actin cytoskeleton. The observation that both lysosomes and KIF17-driven peroxisomes stall at actin patches excludes the possibility for a "tug of war" as a pausing mechanism. The remaining options are "passive" stalling due to physical hindrance, or "active" stalling due to activation of associated actin-binding proteins such myosin motors. As we found no evidence for neuronal peroxisomes associating with the processive myosins V and VI, and, in contrast to lysosomes, LatA treatment did not affect pause duration of peroxisomes, we decided to investigate whether these myosins might be the responsible factor to induce active stalling of lysosomes in dendrites.

Myosin Va, but not Myosin VI, contributes to lysosome stalling

The processive myosins V and VI are known to mediate cargo trafficking in spines. Since lysosomes can be found both in dendrites and dendritic spines (Goo et al, 2017), we asked if lysosomes are associated with myosins and whether this contributes to stalling at actin-rich loci within dendrites. Imaging of fixed lysosomes, enriched from rat cortex and hippocampus, confirmed the presence of the lysosomal markers LAMP1 and LysoTracker (Figure 7A). Immunostaining for the processive myosins Va and VI labeled the same structures as LAMP1 (Figure 7B). Additionally, western blotting of the lysosome-enriched fraction showed the presence of known lysosome-associated MT motor proteins (KIF5C and dynein IC1/2) (Caviston et al, 2011; Farias et al, 2017) as well as myosin Va and myosin VI (Figure 7C). These results point to the possibility that, in addition to actin patches posing as physical barriers, myosins could take over kinesin- or dynein-driven lysosomes and actively stall them once they encounter F-actin-rich environments. To test this hypothesis, we employed a dominant negative approach to inhibit myosin V and VI. Overexpression of a dimerized tail construct of myosin Va (myoV DN), containing the cargo binding domain, is frequently used to impair the function of endogenous myosin Va by competition (González-Gallego et al, 2019; Balasanyan & Arnold, 2014; Correia et al, 2008). Additionally, in live imaging experiments of DIV16-17 neurons overexpressing mCerulean-labelled myoV DN, visible associations between the myoV DN tail and LAMP1-positive vesicles suggested that lysosomes might associate with myosin V motors in living cells (Figure 7D).

Kymograph analysis of LAMP1-mCherry-labelled lysosomes showed that upon overexpression of myoV DN, lysosome motility increased, as judged by the decrease in time spent being stationary (Figure 7E, G) and in pausing time distribution shifted to shorter pauses (Figure 7H). The total number of mobile and stationary lysosomes, as well as instant velocity and instant run length, were not affected (Figure 7F, S3A, B). In a complementary set of experiments, we used a pharmacological inhibitor of myosin V, MyoVin, which partially inhibits the actin-activated ATPase activity of myosin V, thus turning it from a motor into a tether (Gramlich & Klyachko, 2017; Heissler et al, 2017). 30 min of MyoVin treatment (30 µM) increased the number of stationary lysosomes, the total time of long pausing events (>1 min) and the summed pausing time (Figure EV5A-E), while the total time of short pauses (<1 min) and instant velocity decreased (Figure EV5F). In general, we interpret these effects as MyoVin treatment leading to an elongation of the pausing time of lysosomes that are already stalled. The results from MyoV DN and MyoVin together suggest that myosin V can elongate, but not initiate the pausing time of lysosomes.

Next, we asked whether myosin VI might also be involved in the stalling of lysosomes in dendrites. To test this, we used a dominant negative construct, analogous to myoV DN, consisting of the C-terminal cargo binding domain of myosin VI (myoVI DN) fused to GFP (González-Gallego et al, 2019). Kymograph analysis of lysosomal motility in myoVI DN expressing neurons showed only a minimal change in pausing time distribution while all other analyzed parameters were unaffected (Figure 7I-K; S3C, D). We subsequently employed a pharmacological myosin VI inhibitor, 2,4,6-triiodophenol (TIP) (Heissler et al, 2012) to test whether interference with myosin VI actin-activated ATPase activity can affect pausing of lysosomes. We found that TIP treatment slightly increased the fraction of long pauses (> 1 min) and reduced instant velocities and the run length (Figure EV5G, I, L). The pausing behavior, analyzed by summed pausing time as well as relative frequency distribution, was not changed (Figure EV5J, K). We therefore conclude that myosin VI contribution to lysosome stalling is negligible.

All in all, we show that a multitude of factors, both passive and active, are involved in lysosome positioning at the actin patches. The effects of LatA on KIF17-coupled peroxisome transport suggest that the presence of a dense actin-mesh constitutes a passive, physical barrier for kinesin-mediated trafficking. In the presence of actin patches, peroxisomes, which are not associated with myosin V, take frequent but short pauses. Lysosomes, which do contain myosin V, decrease their stalling time upon inhibition of myosin V, and increase their pausing time when myosin V is blocked in F-actin bound position. From this we conclude that actin patches act as a physical hindrance that initially causes cargo to stall indiscriminately. This short stop might be sufficient for other factors to initiate active anchoring and longer stallings. It appears that myosin V but not myosin VI activity allows lysosomes to stop over longer periods of time, but neither of these myosins alone seem to be absolutely essential for the stalling of lysosomes in dendrites.

Discussion

In this study we aimed to obtain a better insight into the factors that define organelle localization in dendrites. We applied STED nanoscopy, pharmacological and cargo trafficking assays to investigate the structural organization of the dendritic cytoskeleton, and asked how its architecture influences the trafficking of organelles using the example of lysosomes as vesicular organelles.

In differentiating neurons, small actin patches present in dendrites serve as places for preferred filopodia outgrowth (Korobova & Svitkina, 2010). Here, we investigated the presence and

function of actin patches in dendrites of mature neurons. We found that the majority was spread over the dendritic shaft, is positive for excitatory but not inhibitory synaptic markers, and their size depends on the presence of homer1. In comparison to spine synapses, the role and organization of the actin cytoskeleton at shaft synapses has not yet been addressed (Bosch et al, 2014; Konietzny et al, 2017; Mikhaylova et al, 2018). Using pharmacological approaches, we found that the actin mesh consisted of both branched and longitudinal filaments. The nucleation and maintenance of the actin patches was independent from endosomes, which makes them distinct from the axonal actin hotspots (Ganguly et al, 2015). The actin turnover rates at the dendritic patches are very similar to those at the dendritic spines. These observations strongly suggest that the dendritic actin patches are part of excitatory shaft synapses. Moreover, these shaft synapses presumably contribute to synaptic signalling as they are opposed to active presynaptic terminals, and are positive for both AMPA and NMDA receptors.

Dendritic microtubules shape around these dendritic actin patches, but do not invade. We therefore speculate that actin patches form strong physical barriers for newly growing microtubules, forcing them to go around. Along the same lines, the rigidity of actin patches at the base of spines could contribute to redirect growing microtubules into spines (Schätzle et al, 2018). Interestingly, we noticed that in contrast to F-actin patches, MT bundles were closely associated with the periodic F-actin lattice in dendrites. Indeed, it has been shown that at least in the axon, periodic actin structures are required to maintain microtubules (Qu et al, 2017). That points to a very different nature and molecular environment of those two types of F-actin structures.

In another recent work we used quantum dots to study the heterogeneity of the cytoplasm and demonstrated that the F-actin-rich cellular cortex at the inner face of the plasma membrane is able to trap diffusive probes of a certain size (Katrukha et al, 2017). The presence of a dense actin mesh in dendrites might therefore influence the diffusion of molecules by confining local environments, and directly or indirectly influence organelle transport. An interesting question is how vesicular organelles like lysosomes behave in actin-rich areas. In recent years, several studies have demonstrated a role of lysosomes in synaptic plasticity (Goo et al, 2017; Padamsey et al, 2017). In addition to the classical degradation function, lysosomes can release their content into the extracellular space via Ca^{2+}-dependent exocytosis, which is an important mechanism allowing remodeling of the extracellular matrix in proximity to activated spines (Padamsey et al, 2017). Such a mechanism would require active control of lysosomal localization within dendrites, which could also apply to other vesicular organelles.

Here we used LysoTracker and LAMP1 to label lysosome-related compartments and observed that the labeled vesicles could be divided into stationary and mobile fractions, with the latter being moved bidirectionally in dendrites. STED imaging indicated that lysosomes can be trapped deep inside actin patches or be localized near the borders. Similarly to Goo et al., we found that treatment with the F-actin depolymerizing agent LatA reduced the fraction of stationary lysosomes (Goo et al, 2017). Interestingly, at basal conditions there was some bias towards anterograde trafficking of lysosomes, which was diminished upon LatA treatment. This effect could be due to differential effects of the F-actin mesh on cargoes powered by different types of microtubule motors. Moreover, while performing life imaging experiments, we found that lysosomes frequently stop at actin patches. Retention of organelles at actin patches can be passive, as they form physical barriers within dendrites, or an active process, in which myosin motors or potentially other actin binding proteins bind to the F-actin. In addition, a complex interplay between the activities of different MT motors attached to the same vesicle could affect cargo transport in proximity to F-actin patches.

To test if the F-actin mesh at the shaft synapse could serve as a passive organelle trap we designed a cargo-motor controlled assay, in which usually immobile peroxisomes were used as an artificial cargo for a constitutively active KIF17 motor. This organelle probe allowed us to rule out a “tug of war” between different types of MT motors attached to the same cargo. Analysis of peroxisomal movement in dendrites demonstrated that, at least to some extent, purely kinesin-driven organelles can be stalled at F-actin rich areas. This indicates that the F-actin mesh can be an obstacle for MT-motor driven vesicular organelle transport.

Next, we tested a potential contribution of the processive motors myosin V and VI in lysosome stalling. They are known to mediate cargo transport into and inside dendritic spines (Correia et al, 2008; Esteves da Silva et al, 2015) and dendritic cargo sorting at the axon initial segment is based on the presence of myosin V (Janssen et al, 2017). Thus it is very likely that many dendritic cargos are associated with myosins. Enriched lysosomes from rat brains, indeed, appeared to associate with myosin Va and VI. We explored their contribution to pausing events of lysosomes by combining dominant negative forms of myosin with pharmacological approaches. Dominant negative inhibition of myosin V led to a reduction of stalling time, whereas inhibition of myosin VI had very little to no effect. We therefore speculate that within dendrites the trafficking of endo-lysosomal/vesicular organelles is affected by the presence of F-actin patches, via both passive stalling and activation of specific actin binding proteins, including myosin V.

The Ca^{2+}/calmodulin dependency of myosin V activation could provide a mechanism for activity-dependent positioning of lysosomes (Goo et al, 2017; Wang et al, 2008). It is conceivable that only a subset of lysosomes will carry myosins, possibly depending on their maturation status. In a recent study, Cheng and colleagues performed a rigorous characterization of LAMP1-positive compartments in dendrites. They found that about half of the LAMP1-labelled structures contained functional lysosomal proteases cathepsin B and D, markers for mature lysosomes (Cheng et al, 2018). It has also been shown that neuronal activity induces lysosomal exocytosis and release of cathepsins (Padamsey et al, 2017). The spatially and temporally controlled cathepsin B release from mature lysosomes may be a critical step required for input-specific synaptic potentiation. The close proximity to NMDA receptors at shaft synapses would allow for direct Ca^{2+}-dependent synaptic control of lysosomal exocytosis. A dense actin mesh surrounding the PSD of shaft synapses or at the base of spines could stall mature fusion-competent lysosomes for longer periods. Alternatively, long pausing events might promote endolysosomal maturation. How trafficking rules relate to lysosomal maturation needs to be addressed in future studies.

The finding that most actin patches are part of active excitatory shafts synapses raises many new exiting questions. In contrast to spine synapses, the organization, stability and function of excitatory shaft synapses remain largely unexplored. Some studies indicate that during neuronal development, shaft synapses are precursors for spine synapses, while others suggest that they comprise an independent category of synapses, also in the mature brain (Aoto et al, 2007; Bourne & Harris, 2011; Reilly et al, 2011). It is interesting to know if and how activation of shaft synapses influences organelle transport. Opening of NMDA receptors at shaft synapses will lead to direct influx of calcium into the dendritic shaft. Shaft synapses might therefore contribute more strongly to controlling organelle trafficking in comparison to spine synapses, since they lack the spatial confinement by a spine neck (Sabatini et al, 2002). We anticipate that dense dendritic actin patches could also limit molecule diffusion and encourage local confinement. Calcium influx at a shaft synapse could result in local dendritic areas with changed traffic signals, allowing for coordinated cargo delivery and positioning in places of high demand. Moreover, the size and density of the F-actin mesh at shaft synapses or actin patches at the spine base could be rapidly altered by synaptic activation, providing a fine-tuning of its size and complexity.

In summary, dendritic trafficking of organelles is complex and involves many parameters including the architecture of the cytoskeleton, associated motor proteins and synaptic activity.

Here we looked deeply into the cytoskeletal architecture using super resolution microscopy and live cell imaging techniques. The results illustrate that dendritic actin patches, at spine bases and at shaft synapses, can influence organelle trafficking. Whether these F-actin patches could serve as a hub for bringing organelles in proximity to each other, promoting organelle-organelle contact, and how this relates to organelle functioning and maturation e.g. during plasticity events, deserves further investigation.

Materials and Methods

Animals

Wistar rats Crl:WI(Han) (Charles River) and Wistar Unilever HsdCpb:WU (Envigo) rats were used in this study. Sacrificing of pregnant rats (E18) for primary hippocampal cultures, P7 male rat pups for organotypic slice cultures and adult female rats for biochemistry was done in accordance with the Animal Welfare Law of the Federal Republic of Germany (Tierschutzgesetz der Bundesrepublik Deutschland, TierSchG) and with the approval of local authorities of the city-state Hamburg (Behörde für Gesundheit und Verbraucherschutz, Fachbereich Veterinärwesen, from 21.04.2015) and the animal care committee of the University Medical Center Hamburg-Eppendorf.

Hippocampal neuronal primary cultures, transfections

Rat primary hippocampal cultures were prepared as described previously with slight modifications (Kapitein et al 2010). In short, hippocampi were dissected from E18 embryos, physically dissociated after 10min of trypsin treatment (0.25 %, *Thermo Fisher Scientific*, #25200-056) at 37 °C, and plated on poly-L-lysine (*Sigma-Aldrich*, #P2636) coated glass coverslips (18mm) at a density of 40000-60000 cells per 1ml on in DMEM (*Gibco*, #41966-029) supplemented with 10 % fetal calf serum (*Gibco*, 10270) and antibiotics (*Thermo Fisher Scientific*, #15140122). After 1 h, plating medium was replaced by BrainPhys neuronal medium supplemented with SM1 (*Stem Cell kit*, #5792) and 0.5 mM glutamine (*Thermo Fisher Scientific*, #25030024). Cells were grown in an incubator at 37 °C, 5 % CO_2 and 95 % humidity.

Cultures were transfected at indicated time points using lipofectamine 2000 (*Thermo Fisher Scientific*, #11668019). The DNA/lipofectamine ratio was according to the manufacturer's protocol 1:2. For co-transfection of plasmids the ratios of different constructs were optimized per combination, and optionally by addition of an empty vector (pcDNA3.1), to tune expression levels. Before transfection the original neuronal medium was removed. Neurons were transfected in BrainPhys medium, optionally supplemented with glutamine, but lacking SM1. Transfection medium was added for 45 min – 1.5 h. After transfection, the medium was exchanged back to the original BrainPhys containing SM1. Experiments on transfected neurons were performed 1 day after transfection.

Immunocytochemistry

Primary cultures were fixed with 4% Roti-Histofix / 4% sucrose for 10 min at room temperature (RT), washed 3 x 10 min with phosphate buffered saline (PBS), and permeabilized with 0.2 % Triton X-100 in PBS for 10 min at RT. The cells were then washed 3 x in PBS and blocked for 45 min at RT with blocking buffer (10 % horse serum, 0.1 % Triton X-100 in PBS). Primary antibodies were added in blocking buffer and incubated overnight at 4 °C. Cells were washed 3 x 10 min before addition of secondary antibodies in blocking buffer, and incubation for 1 h at RT. Optionally, phalloidin-Atto647N was added 1:40 in PBS and incubated overnight at 4 °C. Finally, coverslips were washed 3-5 x 10 min in PBS and mounted on microscope slides with mowiol. Mowiol was prepared according to the manufacturer's protocol (9.6 g mowiol 4-88 (*Carl-Roth*), 24.0 g glycerine, 24 ml H_2O, 48 ml 0.2 M Tris pH 8.5, including 2.5 g Dabco, (*Sigma-Aldrich* D27802).

Live cell imaging: wide field, TIRF and spinning disc microscopy

Live cell wide-field and TIRF microscopy was performed with a Nikon Eclipse Ti-E controlled by VisiView software (*VisitronSystems*). Samples were kept in focus with the built-in Nikon perfect focus system. Fluorophores were excited by 488 nm, 561 nm, and 639 nm laser lines, coupled to the microscope via an optic fiber. HILO and TIRF illuminations were obtained with an ILAS2 (*Gataca-systems*) spinning-TIRF system. Samples were imaged with a 100x TIRF objective (*Nikon*, ApoTIRF 100x/1.49 oil). Emission light was collected through a quad-band filter (*Chroma*, 405/488/561/640) followed by a filter wheel with filters for GFP (*Chroma*, 525/50m), RFP (*Chroma*, 595/50m), and Cy5 (*Chroma*, 700/75m). Multi-channel images were acquired sequentially with an Orca flash 4.0LT CMOS camera (*Hamamatsu*). Images were acquired at 2- 5 frames per second or at specified intervals.

FRAP of actin-RFP was performed using the ILAS2 unit. RFP was imaged and bleached using a 561 nm laser. Photo-bleaching was performed with 2 ms per pixel, with an approximate 2 fold laser intensity. Images were acquired with 3 seconds increments in HILO illumination, starting with a 10 frames baseline before FRAP.

Spinning-disc confocal was performed with a Nikon Eclipse Ti-E controlled by VisiView software. Samples were kept in focus with the built-in Nikon perfect focus system. The system was equipped with a 100x TIRF objective (*Nikon*, ApoTIRF 100x/1.49 oil), and 488 nm, 561 nm, and 639 nm excitation laser. Lasers were coupled to a CSU-X1 spinning disk unit via a single-mode fiber. Emission was collected through a quad band filter (*Chroma*, ZET 405/488/561/647m) on an Orca flash 4.0LT CMOS camera (*Hamamatsu*). Images were acquired sequentially with 0.3- 3 frames per second or at specified intervals.

Additional Spinning-disk confocal microscopy was performed with a Nikon Eclipse Ti-E controlled by VisiView software. Samples were kept in focus with the built-in Nikon prefect focus system. 488 nm and 561 nm excitation lasers were coupled to a CSU-W1 spinning-disk unit (*Yokogawa*) via a single-mode fiber. Cells were imaged with either a 60x (*Nikon*, ApoTIRF 60x/1.49) or a 100x (Nikon, CFI plan Apochromat Lambda 100x/1.45) objective. Emission light was split by a 561 LP dichroic and filtered through a GFP (*Chroma*, 525/50m), or a mCherry filter (*Chroma*, 609/34m). Multichannel images were acquired simultaneously on two EM-CCD cameras (*Photometrics*, Evolve 512 Delta). Images were acquired at 4 frames per second.

At all systems, neurons were imaged in regular culture medium. Coverslips were placed in either an attofluor cell chamber (*Thermo Fisher Scientific*) or a Ludin chamber (*Life Imaging Services*). Correct temperature (37 °C), CO_2 (5 %) and humidity (90 %) were maintained with a top stage incubator and an additional objective heater (*Okolab*).

If pharmacological treatment was performed during live imaging, the respective drug was added manually to the culture medium and incubated for the indicated time spans in the top stage incubator.

Confocal, $_{gated}$STED imaging, and deconvolution

Confocal microscopy of fixed primary cultures was performed at a Leica TCS SP5 confocal microscope (*Leica microsystems, Manheim, Germany*). The microscope was controlled by Leica Application Suite Advanced Fluorescence software. Samples were imaged using a 63x oil objective (*Leica*, HC PL APO CS2 63x/1.40 oil). Fluorophores were excited with a 488 nm Argon laser, 561 nm Diode Pumped Solid State laser and a 633 nm HeNe laser. Images were acquired at 1024x1024, with a 60 nm pixel size, in 8 bit. To reduce noise a 2 times frame averaging was applied. For z-stacks, z-step size was set to 0.29 µm.

Fixed organotypic slices were imaged at an Olympus FV1000 confocal microscope with a 40x objective (*Olympus*, UPLFLN 40x/1.3). Fluorophores were excited by a 488 nm and a 559 nm laser line. Pinhole size was set to 80 µm. Excitation and emission light was divided by a quad-band filter (405/488/559/635). Emission light was split by a 570b nm dichroic and filtered through a GFP (495-540 nm) or a RFP (575-630 nm) filter. Images were acquired sequentially with two high sensitivity detectors. Pixel size was 77 nm, with a z-step size of 0.2 µm. Single planes consisted of 3 frame averages, 12-bit.

$_{Gated}$STED images were acquired at a Leica TCS SP8-3X $_{gated}$STED system (*Leica microsystems*) equipped with a pulsed white light laser (WLL) for excitation ranging from 470 to 670 nm. STED was obtained with a 592 nm continuous wave and a 775 nm pulsed depletion laser.

Samples were imaged with either a 100x objective (*Leica*, HC APO CS2 100x/1.40 oil), or a 93x glycerol objective (*Leica*, HC APO 93x/1.30 GLYC motCORR). The refractive index (RI) of mowiol (see immunocytochemistry) polymerized for 3 days was 1.46 (measured with Digital Refractometer AR200 (*Reichert*), and matched the RI of glycerol (1.45) better than oil (1.51). Therefore, when available, the 93x glycerol objective was the preferred objective. For excitation of the respective channels the WLL was set to 650 nm for phalloidin-Atto647N, 561 nm for Abberior Star 580 and oyster550 conjugated secondary antibodies, and 488 nm for either Alexa Fluor 488 conjugated secondary antibodies or GFP-fusion proteins. STED was attained with the 775 nm laser for Atto647N/Abberior 580 and with the 592 nm laser for Alexa Fluor 488/eGFP. Emission spectra were detected at 660-730 nm for Atto647N, 580-620 nm for Abberior Star 580, and 500-530 nm for Alexa Fluor 488 or eGFP. For $_{\text{gated}}$STED, detector time gates were set to 0.5-6 ns for Abberior Star 580/Atto647N and 1.5 ns-6 ns for Alexa Fluor 488/ eGFP. Images were acquired as single planes of either 1024x1024 pixels or 1386x1386, optical zoom factor 5 (for oil: x/y 22.73 nm, for glycerol: x/y 24.44 nm or 18.28nm) or 6 (glycerol x/y 20.37nm), 600 lines per second and 16 x line averaging. Corresponding confocal channels had the same setting as STED channels, except the excitation power was reduced and the detection time gates were set to 300 ps - 6 ns for all channels.

Deconvolution of STED and confocal laser scanning (CLSM) images were done with Huygens Professional (*Scientific Volume Imaging*). Within the *Deconvolution wizard*, images were subjected to a background correction, *Signal-to-noise ratio* was set to 15 for STED and 30 or 40 for CLSM images. *The Optimized iteration mode of the CMLE* was applied until it reached a *Quality threshold of 0.01* for STED and *0.05* for CLSM images.

Kymograph analysis

Kymographs were constructed using the *KymographClear* (Mangeol et al, 2016) or *KymoResliceWide* plugin for Fiji (*NIH*) (Schindelin et al, 2012). Non-overlapping dendritic stretches of 30 – 80 µm length were traced, using the *segmented line* tool. Maximum 3 dendrites were taken from the same neuron. Line thickness was chosen to cover the dendritic shaft, but to omit spines. Trajectories in the kymographs were traced by hand using the *straight line* tool. Trajectories with a uniform speed (= slope) were considered one “event”, changes in speed (= slope) or stopping events (= vertical lines) were traced as separate events (Figure S1). Slope and length of each event were used to calculate instant velocity, instant run length, and pausing time. In general, all lysosomes were analyzed. For experiments with the PEX3-Kif17 construct only

peroxisomes that showed at least one moving behavior were analyzed. Non-moving peroxisomes could be due to inefficient coupling and were therefore excluded.

Data representation and Statistical Analysis

For representative microscopy images brightness and contrast are linearly adjusted per channel. Statistical analysis was performed in Statistica 13 (*Dell Inc.*) or Prism 6.05 (*GraphPad*). Detailed specifications about the type of test, significance levels, n numbers, and biological replicates are provided in the figure legends. Data are represented individually in dot blots or as mean ± SEM throughout the manuscript.

Acknowledgements

The authors would like to thank W. Wagner (*MyosinV-DN_mCerulean*), A.S. Kostyukova (actin-RFP) and T.G. Oertner (mCerulean, mRuby2) for sharing plasmids. Psd95.FingR_eGFP_CCR5TC was a gift from Don Arnold (Addgene plasmid #46295). We thank UMIF for access and use of their spinning-disc and confocal microscopes. This work was supported by grants from the Deutsche Forschungsgemeinschaft (DFG): Emmy-Noether Programm (MI 1923/1-1), FOR2419 (MI 1923/2-1 and MI 1923/2-2), CRC877 (INST 257/602-1) to M.M. and DFG grand SCHE 132/18-1 to O.K.

Author contributions

B.v.B., A.K., J.B., and M.M. designed the study. B.v.B., A.K., O.K., J.B., and M.M. conducted the experiments. B.v.B., A.K., J.B., and M.M. analysed the data. M.M. supervised the project and wrote the manuscript. All authors commented on and revised the manuscript.

Conflict of interest

The authors declare no conflict of interests.

References

Aoto J, Ting P, Maghsoodi B, Xu N, Henkemeyer M, Chen L (2007) Postsynaptic ephrinB3 promotes shaft glutamatergic synapse formation. J Neurosci 27**:** 7508-7519

Aschenbrenner L, Lee T, Hasson T (2003) Myo6 facilitates the translocation of endocytic vesicles from cell peripheries. Molecular biology of the cell 14**:** 2728-2743

Balasanyan V, Arnold DB (2014) Actin and myosin-dependent localization of mRNA to dendrites. PLoS One 9**:** e92349

Bär J, Kobler O, van Bommel B, Mikhaylova M (2016) Periodic F-actin structures shape the neck of dendritic spines. Sci Rep 6**:** 37136

Bosch M, Castro J, Saneyoshi T, Matsuno H, Sur M, Hayashi Y (2014) Structural and molecular remodeling of dendritic spine substructures during long-term potentiation. Neuron 82**:** 444-459

Bourne JN, Harris KM (2011) Coordination of size and number of excitatory and inhibitory synapses results in a balanced structural plasticity along mature hippocampal CA1 dendrites during LTP. Hippocampus 21**:** 354-373

Bowen AB, Bourke AM, Hiester BG, Hanus C, Kennedy MJ (2017) Golgi-independent secretory trafficking through recycling endosomes in neuronal dendrites and spines. Elife 6

Caviston JP, Zajac AL, Tokito M, Holzbaur EL (2011) Huntingtin coordinates the dynein-mediated dynamic positioning of endosomes and lysosomes. Molecular biology of the cell 22**:** 478-492

Cheng XT, Xie YX, Zhou B, Huang N, Farfel-Becker T, Sheng ZH (2018) Characterization of LAMP1-labeled nondegradative lysosomal and endocytic compartments in neurons. J Cell Biol 217**:** 3127-3139

Correia SS, Bassani S, Brown TC, Lise MF, Backos DS, El-Husseini A, Passafaro M, Esteban JA (2008) Motor protein-dependent transport of AMPA receptors into spines during long-term potentiation. Nature neuroscience 11**:** 457-466

D'Este E, Kamin D, Gottfert F, El-Hady A, Hell SW (2015) STED nanoscopy reveals the ubiquity of subcortical cytoskeleton periodicity in living neurons. Cell Rep 10**:** 1246-1251

Esteves da Silva M, Adrian M, Schatzle P, Lipka J, Watanabe T, Cho S, Futai K, Wierenga CJ, Kapitein LC, Hoogenraad CC (2015) Positioning of AMPA Receptor-Containing Endosomes Regulates Synapse Architecture. Cell Rep 13**:** 933-943

Farias GG, Guardia CM, De Pace R, Britt DJ, Bonifacino JS (2017) BORC/kinesin-1 ensemble drives polarized transport of lysosomes into the axon. Proceedings of the National Academy of Sciences of the United States of America 114**:** E2955-e2964

Ganguly A, Tang Y, Wang L, Ladt K, Loi J, Dargent B, Leterrier C, Roy S (2015) A dynamic formin-dependent deep F-actin network in axons. J Cell Biol 210**:** 401-417

González-Gallego J, Konietzny A, Perez-Alvarez A, Bär J, Maier U, Drakew A, Hammer JAI, Demmers JAA, Dekkers DHW, Frotscher M, Kneussel M, Oertner T, Wagner W & Mikhaylova M (2019) Characterization of neuronal synaptopodin reveals a myosin V-dependent mechanism of synaptopodin clustering at the post-synaptic sites. bioRxiv (10.1101/526509)

Goo MS, Sancho L, Slepak N, Boassa D, Deerinck TJ, Ellisman MH, Bloodgood BL, Patrick GN (2017) Activity-dependent trafficking of lysosomes in dendrites and dendritic spines. J Cell Biol 216**:** 2499-2513

Gramlich MW, Klyachko VA (2017) Actin/Myosin-V- and Activity-Dependent Inter-synaptic Vesicle Exchange in Central Neurons. Cell Rep 18**:** 2096-2104

Hancock WO (2014) Bidirectional cargo transport: moving beyond tug of war. Nature reviews Molecular cell biology 15**:** 615-628

Hanus C, Kochen L, Tom Dieck S, Racine V, Sibarita JB, Schuman EM, Ehlers MD (2014) Synaptic control of secretory trafficking in dendrites. Cell Rep 7**:** 1771-1778

Hanus C, Schuman EM (2013) Proteostasis in complex dendrites. Nature reviews Neuroscience 14**:** 638-648

He J, Zhou R, Wu Z, Carrasco MA, Kurshan PT, Farley JE, Simon DJ, Wang G, Han B, Hao J et al (2016) Prevalent presence of periodic actin-spectrin-based membrane skeleton in a broad range of neuronal cell types and animal species. Proceedings of the National Academy of Sciences of the United States of America 113**:** 6029-6034

Heissler SM, Chinthalapudi K, Sellers JR (2017) Kinetic signatures of myosin-5B, the motor involved in microvillus inclusion disease. The Journal of biological chemistry 292**:** 18372-18385

Heissler SM, Selvadurai J, Bond LM, Fedorov R, Kendrick-Jones J, Buss F, Manstein DJ (2012) Kinetic properties and small-molecule inhibition of human myosin-6. FEBS Lett 586**:** 3208-3214

Hlushchenko I, Koskinen M, Hotulainen P (2016) Dendritic spine actin dynamics in neuronal maturation and synaptic plasticity. Cytoskeleton (Hoboken) 73**:** 435-441

Ivanova D, Dirks A, Montenegro-Venegas C, Schone C, Altrock WD, Marini C, Frischknecht R, Schanze D, Zenker M, Gundelfinger ED et al (2015) Synaptic activity controls localization and function of CtBP1 via binding to Bassoon and Piccolo. The EMBO journal 34**:** 1056-1077

Janssen AFJ, Tas RP, van Bergeijk P, Oost R, Hoogenraad CC, Kapitein LC (2017) Myosin-V Induces Cargo Immobilization and Clustering at the Axon Initial Segment. Frontiers in Cellular Neuroscience 11**:** 260

Kapitein LC, Schlager MA, Kuijpers M, Wulf PS, van Spronsen M, MacKintosh FC, Hoogenraad CC (2010) Mixed microtubules steer dynein-driven cargo transport into dendrites. Curr Biol 20**:** 290-299

Katrukha EA, Mikhaylova M, van Brakel HX, van Bergen En Henegouwen PM, Akhmanova A, Hoogenraad CC, Kapitein LC (2017) Probing cytoskeletal modulation of passive and active intracellular dynamics using nanobody-functionalized quantum dots. Nature communications 8**:** 14772

Kim K, Lakhanpal G, Lu HE, Khan M, Suzuki A, Hayashi MK, Narayanan R, Luyben TT, Matsuda T, Nagai T et al (2015) A Temporary Gating of Actin Remodeling during Synaptic Plasticity Consists of the Interplay between the Kinase and Structural Functions of CaMKII. Neuron 87**:** 813-826

Kneussel M, Wagner W (2013) Myosin motors at neuronal synapses: drivers of membrane transport and actin dynamics. Nature reviews Neuroscience 14**:** 233-247

Konietzny A, Bär J, Mikhaylova M (2017) Dendritic Actin Cytoskeleton: Structure, Functions, and Regulations. Frontiers in Cellular Neuroscience 11**:** 147

Korobova F, Svitkina T (2010) Molecular architecture of synaptic actin cytoskeleton in hippocampal neurons reveals a mechanism of dendritic spine morphogenesis. Molecular biology of the cell 21**:** 165-176

Lukinavicius G, Reymond L, D'Este E, Masharina A, Gottfert F, Ta H, Guther A, Fournier M, Rizzo S, Waldmann H et al (2014) Fluorogenic probes for live-cell imaging of the cytoskeleton. Nat Methods 11**:** 731-733

Mangeol P, Prevo B, Peterman EJ (2016) KymographClear and KymographDirect: two tools for the automated quantitative analysis of molecular and cellular dynamics using kymographs. Molecular biology of the cell 27**:** 1948-1957

Matsuzaki M, Honkura N, Ellis-Davies GC, Kasai H (2004) Structural basis of long-term potentiation in single dendritic spines. Nature 429**:** 761-766

Matus A (2000) Actin-based plasticity in dendritic spines. Science 290**:** 754-758

Mikhaylova M, Bär J, van Bommel B, Schätzle P, YuanXiang P, Raman R, Hradsky J, Konietzny A, Loktionov EY, Reddy PP et al (2018) Caldendrin Directly Couples Postsynaptic Calcium Signals to Actin Remodeling in Dendritic Spines. Neuron 97**:** 1110-1125.e1114

Mikhaylova M, Bera S, Kobler O, Frischknecht R, Kreutz MR (2016) A Dendritic Golgi Satellite between ERGIC and Retromer. Cell Rep 14**:** 189-199

Nirschl JJ, Ghiretti AE, Holzbaur ELF (2017) The impact of cytoskeletal organization on the local regulation of neuronal transport. Nature reviews Neuroscience 18**:** 585-597

Padamsey Z, McGuinness L, Bardo SJ, Reinhart M, Tong R, Hedegaard A, Hart ML, Emptage NJ (2017) Activity-Dependent Exocytosis of Lysosomes Regulates the Structural Plasticity of Dendritic Spines. Neuron 93**:** 132-146

Penn AC, Zhang CL, Georges F, Royer L, Breillat C, Hosy E, Petersen JD, Humeau Y & Choquet D (2017) Hippocampal LTP and contextual learning require surface diffusion of AMPA receptors. Nature 549: 384–388

Pu J, Guardia CM, Keren-Kaplan T, Bonifacino JS (2016) Mechanisms and functions of lysosome positioning. J Cell Sci 129**:** 4329-4339

Qu Y, Hahn I, Webb SE, Pearce SP, Prokop A (2017) Periodic actin structures in neuronal axons are required to maintain microtubules. Molecular biology of the cell 28**:** 296-308

Racz B, Weinberg RJ (2013) Microdomains in forebrain spines: an ultrastructural perspective. Molecular neurobiology 47**:** 77-89

Reilly JE, Hanson HH, Phillips GR (2011) Persistence of excitatory shaft synapses adjacent to newly emerged dendritic protrusions. Mol Cell Neurosci 48**:** 129-136

Richter K, Langnaese K, Kreutz MR, Olias G, Zhai R, Scheich H, Garner CC, Gundelfinger ED (1999) Presynaptic cytomatrix protein bassoon is localized at both excitatory and inhibitory synapses of rat brain. The Journal of comparative neurology 408**:** 437-448

Sabatini BL, Oertner TG, Svoboda K (2002) The life cycle of Ca(2+) ions in dendritic spines. Neuron 33**:** 439-452

Schätzle P, Esteves da Silva M, Tas RP, Katrukha EA, Hu HY, Wierenga CJ, Kapitein LC, Hoogenraad CC (2018) Activity-Dependent Actin Remodeling at the Base of Dendritic Spines Promotes Microtubule Entry. Curr Biol 28**:** 2081-2093.e2086

Schindelin J, Arganda-Carreras I, Frise E, Kaynig V, Longair M, Pietzsch T, Preibisch S, Rueden C, Saalfeld S, Schmid B et al (2012) Fiji: an open-source platform for biological-image analysis. Nat Methods 9**:** 676-682

Seipold L, Altmeppen H, Koudelka T, Tholey A, Kasparek P, Sedlacek R, Schweizer M, Bar J, Mikhaylova M, Glatzel M et al (2018) In vivo regulation of the A disintegrin and metalloproteinase 10 (ADAM10) by the tetraspanin 15. Cellular and molecular life sciences : CMLS

Svitkina T, Lin WH, Webb DJ, Yasuda R, Wayman GA, Van Aelst L, Soderling SH (2010) Regulation of the postsynaptic cytoskeleton: roles in development, plasticity, and disorders. J Neurosci 30**:** 14937-14942

Swiatecka-Urban A, Boyd C, Coutermarsh B, Karlson KH, Barnaby R, Aschenbrenner L, Langford GM, Hasson T, Stanton BA (2004) Myosin VI regulates endocytosis of the cystic fibrosis transmembrane conductance regulator. The Journal of biological chemistry 279**:** 38025-38031

Trachtenberg JT, Chen BE, Knott GW, Feng G, Sanes JR, Welker E, Svoboda K (2002) Long-term in vivo imaging of experience-dependent synaptic plasticity in adult cortex. Nature 420**:** 788-794

van Bergeijk P, Hoogenraad CC, Kapitein LC (2016) Right Time, Right Place: Probing the Functions of Organelle Positioning. Trends in cell biology 26**:** 121-134

van Bommel B, Mikhaylova M (2016) Talking to the neighbours: The molecular and physiological mechanisms of clustered synaptic plasticity. Neuroscience and biobehavioral reviews 71**:** 352-361

Wang Z, Edwards JG, Riley N, Provance DW, Jr., Karcher R, Li XD, Davison IG, Ikebe M, Mercer JA, Kauer JA et al (2008) Myosin Vb mobilizes recycling endosomes and AMPA receptors for postsynaptic plasticity. Cell 135**:** 535-548

Xu K, Zhong G, Zhuang X (2013) Actin, spectrin, and associated proteins form a periodic cytoskeletal structure in axons. Science 339**:** 452-456

Conventions and Abbreviations

AMPA - α-amino-3-hydroxy-5-methyl-4-isoxazolepropionic acid

CLSM - confocal laser scanning microscopy

ERGIC - endoplasmic reticulum to Golgi intermediate compartment

F-actin - filamentous actin

FRAP – fluorescence recovery after photobleaching

LatA - latrunculin A

MT - microtubule

myoV/VI DN – myosin V/VI dominant negative

NMDA - N-methyl-D-aspartate

PBS - phosphate-buffered saline

PEX - peroxisome

PSD - postsynaptic density

Px - pixel

STED - stimulated emission depletion

TIP - 2,4,6-triiodophenol

TTX - tetrodotoxin

WLL - white light laser

Figure legends

Figure 1 - Actin patches at dendritic shafts are opposed by presynaptic terminals

A. Deconvolved STED image of a DIV17 hippocampal primary neuron stained with phalloidin-Atto647N showing the dendritic actin cytoskeleton. The arrows indicate examples of F-actin enriched areas, "actin patches", which can be found both at the base of dendritic spines (yellow arrows) and within dendritic shafts (white arrows). Scale bar: 2 µm.

B. Confocal and deconvolved STED image showing the colocalization of phalloidin and actin-chromobody, which label identical F-actin structures. TagBFP was expressed as cell-fill. Scale bar: 2 µm.

C. Deconvolved STED images showing F-actin and the presynaptic protein bassoon. The staining shows that presynaptic boutons oppose actin patches at dendritic shafts (arrows). Scale bar: 2 µm.

Figure 2 - The majority of actin patches are positive for excitatory synapse markers and form functional synaptic contacts

A. Confocal and deconvolved STED images of a DIV16 primary hippocampal neuron showing F-actin (phalloidin-Atto647N; STED), homer1 (STED) and gephyrin (confocal). Homer1 (excitatory synapse marker) and gephyrin (inhibitory synapse marker) indicate postsynaptic sites at the dendritic branch. Zoom in 1 and 2 show homer1 associated with dendritic actin patches. Zoom 3 shows gephyrin which is not associated with a dendritic actin patch. Scale bar: 2 µm, 1 µm (zoom in).

B. Normalized intensity profiles along the dendritic branch (line shown in panel **A**).

C. Confocal and deconvolved STED images of a DIV17 primary hippocampal neuron transfected with tagBFP as cell-fill. Zoom-ins show gephyrin non-associated with actin patch (1), actin patches associated with homer1 (2), and single actin patches (3) located within the dendritic shaft. Scale bar: 2µm, 1 µm (zoom in).

D. Description of co-localization shown in A-C. The majority of actin patches co-localize with the excitatory synapse marker homer1 (65%), a few overlap with gephyrin (12.5 %) or are

negative for both markers (21.5 %). *n = 30 dendritic segments of 19 cells in 2 independent cultures.*

E. Description of actin patches density along dendritic segments with relation to their location at the spine base or within dendritic shafts. *Same n as in D.*

F. Frequency distribution of actin patch sizes, with or without homer1, with relation to their location at the spine base or within dendritic shafts. Dendritic actin patches within the dendritic shaft are generally larger when they contain homer1. Mann-Whitney U-test. *** p<0.001. *n=59 (shafts associated w/o homer1), n=101 (shaft associated w homer1), n=40 (spine associated w/o homer1), n=38 (spine associated w homer1) patches from 27 analyzed dendritic segments of 22 cells in 2 independent cultures.*

G. Confocal images of a DIV17 primary hippocampal neuron stained for F-actin (phalloidin) and homer1 after live uptake of α-synaptotagmin 1 antibodies by active presynaptic terminals. The presynaptic release sites show co-localization with actin patches within dendritic shafts (indicated by yellow circles). Synaptic contacts on spines are indicated by white circles. Silencing of neuronal activity by TTX application reduces synaptic release, and thereby synaptotagmin labeling. Scale bar: 2 µm.

H. Quantification of synaptotagmin antibody uptake shown in **G**.

Left: Normalized synaptotagmin intensity measured in ROIs. Mann-Whitney U-test. * p=0.045. *n=8 (basal), n=5 (TTX) analyzed images with each 16-82 synapses per image from 1 culture.*

Right: Frequency distribution of synaptotagmin intensity of individual synapses. TTX treatment significantly decreases the intensity. 2-tailed Mann-Whitney U-test. *** p<0.001. n=303 (basal), n=132 (TTX) synapses.

I. Maximum intensity projections of confocal image stack of YFP transfected DIV17 hippocampal primary neurons neurons stained for bassoon (presynaptic marker), GluA1- and GluN1-subunits. GluA1 and GluN1 show the presence of AMPA and NMDA receptors (excitatory synapse marker) on the dendritic shaft. Co-localization indicates the presence of excitatory shaft synapses (circles). Scale bar: 5 µm.

Figure 3 - Actin patches have a high actin turnover rate and contain both branched and linear filaments

A. Representative STED and confocal images of DIV21 rat hippocampal neurons treated with either DMSO (solvent control) for 2 h, the G-actin sequestering agent latrunculin A (LatA, 5 µM) for 0.5 h, an Arp2/3 inhibitor (CK-666, 50 µM) for 2 h, or a formin inhibitor (SMIFH2, 30 µM) for 1.5 h, and labelled for the dendritic microtubule marker MAP2, cortactin and phalloidin-Atto647N. Zoom-ins show higher magnification image with arrow pointing to actin patches. LatA leads to the depolymerization of most, but not all, actin patches, indicating the presence of stable and non-stable actin pools within patches. Scale bar: 2 µm, 1 µm (zoom in).

B. Quantification of actin patches density along dendritic segments as shown in (**A**), with relation to their location at the spine base or within dendritic shafts. Pharmacological treatments reduced the number of spine- and shaft-associated actin patches. The reduction in both CK-666 and SMIFH2 treated samples suggest a mixed organization of branched and longitudinal actin filaments. 1-way ANOVA with Dunnett's post hoc test. * p=0.01, ** p=0.002, *** p<0.001. *n= 36 (ctr), n= 21 (LatA), n=22 (CK666), n=16 (SMIFH2) dendritic segments of 23 (ctr), 18 (LatA), 19 (CK666), 15 (SMIFH2) cells in 3 independent experiments*.

C. Correlation of actin patches co-localizing with cortactin as shown in (**A**). The amount of cortactin correlates with the actin intensity for both spine- and shaft-associated actin patches (in DMSO control group). Data is plotted on a logarithmic scale. Pearson correlation. *n=67 (spine associated), n=132 (shaft associated) patches in 20 dendrites of 13 cells in 2 independent experiments*.

D. Representative time-series of a FRAP experiment with a DIV16 primary hippocampal neuron expressing actin-RFP. Arrows indicate fluorescence recovery photo-bleached actin-RFP in a shaft-associated actin patch (red arrow) and actin inside a dendritic spine head (blue arrow). Scale bar: 2µm.

E. Quantification of FRAP of actin-RFP in actin patches and spines as shown in (**D**). Both actin structures display very similar recovery kinetics, indicating that shaft-associated actin patches, like spines, contain a mobile and stable actin pool. *n=118 (actin patches), n=129 (spines) from 26 cells in 2 independent cultures.*

Figure 4 - Spatial organization of F-actin, microtubules and lysosomes in dendrites.

A. Representative deconvolved STED images of a DIV16 primary hippocampal neuron stained with phalloidin-Atto647N and α-tubulin, showing that MTs and F-actin patches are spatially segregated. Arrows indicate examples of F-actin patches in dendritic shafts (white) or F-actin rings in the spine neck (yellow). Note that MTs close to the periodic F-actin lattice in the dendrite do not show this kind of spatial separation (periodic grid). Scale bar: 2 µm.

B. Confocal and 3-color STED images of a DIV17 primary hippocampal neuron stained with phalloidin-Atto647N, α-tubulin and α-LAMP1 antibodies. Zoom-ins shown in high magnification depict examples where lysosomes are located at the interface between F-actin and MTs (1, 4), associated with MTs (2) or embedded into the F-actin mesh (3). Scale bar: 5 µm, 0.5 µm (zoom in).

Figure 5 - Latrunculin A treatment leads to an increased mobility of lysosomes

A. Representative image and kymographs of a time lapse series from a dendritic segment of a DIV17 hippocampal neuron labelled with the cell-permeable lysosomal marker LysoTracker Green, before (control) and after treatment with LatA (5 µM). See also Movie 2 and Figure S1. Scale bars: 5 µm, 10 s.

B. Quantification of lysosome motility from kymographs as shown in (**A**). Analyzed were the total time spent pausing (< 1 min), stationary (≥ 1 min), or moving in the anterograde or retrograde direction. LatA treatment (5 µM) increased the mobile retrograde fraction and decreased the stationary fraction. RM-2-ANOVA with behavior of lysosomes and treatment as within group factors. $F(3, 21)=9.2168$, $p=0.0004$, Newman Keuls post hoc test: * $p=0.049$, *** $p=0.00056$. *n= 8 dendritic segments of 6 cells in 3 independent cultures.*

C. Summed total pausing time of lysosomes (LysoTracker) in LatA treated neurons, relative to the before-treatment control. LatA treatment (5 µM) decreased pausing times of lysosomes. 1-sample t-test against 100 %. * $p=0.01$. *Same n as in B.*

D. Cumulative frequency of the duration of pausing events. LatA treatment (5 µM) led to a shift towards shorter pausing times. 2-tailed Mann-Whitney U-test. * $p=0.015$. *n=48 (pausing events) in 8 dendritic segments of 6 cells in 3 independent cultures.*

E. Analysis of the directional net flux of lysosomes (LysoTracker). LatA treatment (5 µM) abolished the bias towards anterograde flux. 2-tailed paired Student's t-test. * p=0.02. *Same n as in B.*

F, G. Analysis of the instant velocity and the instant run lengths of lysosomes (LysoTracker) moving in the anterograde or retrograde direction. LatA treatment (5 µM) did not significantly affect either of these parameters. 2-tailed paired Student's t-test. *Same n as in B.*

H. Representative image and kymographs of a time lapse series from a dendritic segment of a DIV16 hippocampal neuron transfected with LAMP1-eGFP, before (control) and after treatment with LatA (5 µM). Scale bars: 5 µm, 10 s.

I. Quantification of lysosome motility from kymographs as shown in (**H**). Analyzed were the total time spent pausing (< 1 min), stationary (≥ 1 min), or moving in the anterograde or retrograde direction. LatA treatment (5 µM) increased the mobile retrograde and anterograde fractions and decreased the stationary fraction. RM-2-ANOVA with behavior of lysosomes and treatment as within group factors. F(3, 18)=16.912, p=0.00002. Newman Keuls post hoc test: * p=0.04, ** p=0.005, *** p=0.0002. *n= 7 dendritic segments of 7 cells in 2 independent cultures.*

J. Summed total pausing time of lysosomes (LAMP1) in LatA treated neurons, relative to the before-treatment control. LatA treatment (5 µM) decreased pausing time of lysosomes. 1-sample t-test against 100 %. p=0.008. *Same n as in I.*

K. Cumulative frequency of the duration of pausing events. LatA treatment (5 µM) did not significantly change the distribution of pausing events compared to control. 2-tailed Mann-Whitney U-test. *n=163 (ctr), n=117 (LatA) pausing events in 7 dendritic segments of 7 cells in 2 independent cultures.*

L. Analysis of the directional net flux of lysosomes (LAMP1). Similar to the LysoTracker Green experiments (**C**), LatA treatment (5 µM) abolished the bias towards anterograde flux. 2-tailed paired Student's t-test. ** p=0.003. *Same n as in I.*

M, N. Analysis of the instant velocity and the instant run lengths of lysosomes (LAMP1). LatA treatment (5 µM) increased the average instant run length in the retrograde direction. 2-tailed paired Student's t-test. *** p=0.001. *Same n as in I.*

Figure 6 - Lysosomes stall at dendritic actin patches

A. Representative spinning-disk confocal image and kymograph of a time-lapse series of a DIV17 hippocampal neuron transfected with the F-actin probe chromobody-tagRFP and the lysosomal marker LAMP1-eGFP. Blue arrows indicate stationary vesicles. White arrows indicate pausing events at actin patches. See also Movie 2. Scale bar: 2 µm, 10 c.

B. Quantification of lysosome motility inside and outside actin patches. The average speed of lysosomes was reduced inside actin patches, due to pausing. As a control, randomization of the actin patch locations ("offset", as shown in Figure S2) did not give a significant result, elucidating a correlation between the location of actin patches and a reduced average speed of LAMP1 positive organelles. 2-tailed paired Student's t-test. *** p=0.0004. *n=15 dendritic segments of 11 cells in 3 independent cultures.*

C. Representative spinning-disk confocal image and kymograph of a time-lapse series of a DIV16 hippocampal neuron transfected with chromobody-tagRFP and PEX-GFP-KIF17 (see also EV4C). The kymograph shows that KIF17-coupled peroxisomes frequently stall at actin patches. White arrows indicate stopping events at actin patches. See also Movie 3. Scale bar: 2 µm, 10 s.

D. Quantification of KIF17-coupled peroxisome motility inside and outside actin patches. The average speed of KIF17-bound peroxisomes was not significantly different inside actin patches. As a control, randomization of the actin patch locations ("offset", as shown in Figure S2) was used. 2-tailed paired Student's t-test. *n=17 dendritic segments of 12 cells in 3 independent cultures.*

E. Representative kymograph from a DIV16 hippocampal neuron expressing PEX-GFP-KIF17 before and after LatA treatment (5 µM) (see also **EV4C-E)**. Scale bar: 5 µm, 15 s.

F. Quantification of KIF17-coupled peroxisome motility from kymographs, as in **E**. Analyzed were the total time spent pausing (< 1 min), stationary (≥ 1 min), or moving in the anterograde or retrograde direction. LatA treatment (5 µM) did not significantly affect motility. RM-2-ANOVA with PEX behavior and treatment as within group factors. $F(3, 63)=1.9052$, $p=0.138$. *n=22 dendritic segments of 15 cells in 3 independent cultures.*

G. Summed total pausing time of KIF17-coupled peroxisomes in LatA (5 µM) treated neurons, relative to the before-treatment control. LatA treatment significantly reduced the cumulative pausing time. 1-sample t-test against 100 %. ** p=0.0013. *Same n as in F.*

H. Cumulative frequency of the duration of pausing events of KIF17-coupled peroxisomes before (control) and after LatA treatment (5 µM). LatA treatment did not have a significant effect on the distribution of pausing events. 2-tailed Mann-Whitney U-test. *n=695 (control), n= 579 (LatA) pausing events in 22 dendritic segments of 15 cells in 3 independent cultures.*

I, J. Analysis of the instant velocity and the instant run lengths of KIF17-coupled peroxisomes. LatA treatment (5 µM) decreased the average instant velocity in the anterograde direction and reduced the instant run length in the reterograde direction. I) 2-tailed paired Student's t-test. ** p=0.0012 (I) and 2-tailed Wilcoxon matched pairs test. * p=0.01 (J). *n=22 (anterograde), n=21 (retrograde) dendritic segments of 15 cells in 3 independent cultures.*

Figure 7 - Processive myosins associate with lysosomes and myosin V affects motility of lysosomes in dendrites

A, B. Representative TIRF images of lysosomes enriched from adult rat cortex and stained with LysoTracker Red and α-LAMP1 antibody (A, scale bar: 5 µm), and α-LAMP1 and α-myosin Va / myosin VI antibody (B, Scale bar: 2 µm).

C. Western blot of cleared cortical lysate (input) and enriched lysosome fraction stained with antibodies against myosin Va (myoVa), myosin VI (myoVI), LAMP1, KIF5C and dynein IC 1/2 shows the presence of different motor proteins in the lysosome fraction.

D. Dendritic segment of a DIV16 primary neuron transfected with myoV DN-mCerulean and LAMP1-mCherry. Arrows indicate myoV DN enriched at LAMP1 vesicles. Scale bar: 10 µm.

E. Representative kymographs from dendritic segments of DIV16 primary hippocampal neurons expressing LAMP1-mCherry and either mCerulean (control) or a myoV DN-mCerulean. Scale bar: 5 µm, 15 s.

F. Quantification of mobile and stationary lysosomes. Overexpression of myoV DN did not significantly change lysosome count. Unpaired 2-tailed Student's t-test (mobile) or Mann-Whitney U-test (stationary). *n=30 (ctr), n= 28 (DN) analyzed dendritic segments from 21 cells in 3 independent cultures.*

G. Quantification of lysosome motility from kymographs as shown in **E**. Analyzed were the total time spent pausing (< 1 min), stationary (≥ 1 min), or moving in the anterograde or retrograde direction. Overexpression of myoV DN led to an increase in pausing events and decreased the number of stationary lysosomes. RM-2-ANOVA with behavior of lysosomes as within group factor and myoV DN as categorical factor. $F(3, 174)=6.1977$, $p=0.0005$ with Newman Keuls post hoc test: * $p<0.05$, *** $p=0.0003$. *Control: n=31 dendritic segments of 21 cells in 3 independent experiments. MyoV DN: n = 29 analyzed dendritic segments from 21 cells in 3 independent cultures.*

H. Cumulative frequency of the duration of pausing events of lysosomes (LAMP1-mCherry) in control (mCerulean) and myoV DN-mCerulean expressing neurons. Fully stationary events are excluded. Presence of myoV DN led to a shift towards shorter pausing events. 2-tailed Mann-Whitney U-test. *** $p<0.001$. *n=836 (control) pausing events in 31 dendritic segments of 21 cells, n=973 (myoV DN) pausing events in 29 dendritic segments of 21 cells in 3 independent cultures.*

I. Representative kymographs from dendritic segments of DIV16/DIV17 primary hippocampal neurons expressing LAMP1-mCherry and either YFP (control) or a myoVI DN-GFP construct. Scale bar: 5 µm, 15 s.

J. Quantification of mobile and stationary lysosomes. Overexpression of myoVI DN did not have a significant effect on lysosome count. 2-tailed Mann-Whitney U-test. *n=20 (ctr), n= 25 (DN) dendritic segments of 20 cells (control) and 23 cells (myoVI DN) in 2 independent cultures.*

K. Quantification of lysosome motility from kymographs as shown in **I**. Analyzed were the total time spent pausing (< 1 min), stationary (≥ 1 min), or moving in the anterograde or retrograde direction. Overexpression of myoVI DN did not cause significant changes. RM-2-ANOVA with behavior of lysosomes as within group factor and myoVI DN as categorical factor. $F(3, 129)=0.25$, $p=0.86$. *Same n as in J.*

L. Cumulative frequency of the duration of pausing events of lysosomes (LAMP1-mCherry) in control (YFP) and myoVI DN-GFP expressing neurons. Fully stationary events are excluded. Presence of myoVI DN led to a shift towards longer pausing events. 2-tailed Mann-Whitney U-test. ** $p=0.009$. *n=838 (control) in 20 dendritic segments of 20 cells, n=853 (MyoVI DN) pausing events in 25 dendritic segments of 23 cells in 2 independent cultures.*

Expanded View Figures:

Figure EV1 - Appearance of dendritic actin patches coincides with the development of synapses and maturation of primary cultures

A. Confocal image of the dendritic segment shown in Figure **1A**. The segment is positive for the microtubule dendritic marker MAP2. The arrows indicate examples of actin patches at the base of dendritic spines (yellow arrows) and within the dendritic shaft (white arrows). Scale bar: 2 µm.

B. Representative confocal images of the development of primary hippocampal cultures and zoom-in of a dendritic segment. Actin patches appear together with the development of presynaptic sites, positive for bassoon. Arrows indicate actin patches. Scale bar: 50 µm, 10 µm (zoom in).

C. Confocal image of a hippocampal neuron stained for MAP2, bassoon, and F-actin labeled with phalloidin-Atto647N. The ROI indicates the dendritic segment shown in Figure **1C**. Scale bar: 10 µm.

Figure EV2 - Excitatory shaft synapses in hippocampal primary and slice cultures

A. Upper panel: Maximum projection of a confocal image stack of a primary hippocampal neuron at DIV17, transfected with mRuby2 (cell-fill) and FingR-PSD95-eGFP as an excitatory postsynaptic marker, and stained for bassoon as a presynaptic marker. Lower panel: Higher magnification image and corresponding 3D-reconstruction show the presence of excitatory shaft synapses (arrows). Images are presented with a 1 px Gaussian blur filter. Scale bar: 10 µm, 5 µm.

B. Upper panel: Maximum projection of a confocal image stack displaying the apical dendrite of a CA1 pyramidal neuron in a hippocampal slice culture at DIV18, electroporated with mRuby2 (cell-fill) and FingR-PSD95-eGFP as excitatory postsynaptic marker. Lower panel: 3D-reconstruction demonstrated the presence of excitatory shaft synapses (red). Images are presented with a 1 px Gaussian blur filter. See also Movie 1. Scale bar: 10 µm, 5 µm (zoom in).

C. Quantification of actin patch size in control (DMSO), LatA (5 µM for 30 min), CK666 (50 µM for 2 h), and SMIFH2 (30 µM for 90 min) treated neurons. Patch size for spine associated patches is not significantly changed after treatment. The size of shaft associated patches was

reduced after LatA treatment. 1-way ANOVA with Dunnett's post hoc test. * p=0.02. n=71 *(ctr), n=10 (LatA), n=31 (CK666), n=11 (SMIFH2) spine associated patches and n=151 (ctr), n=95 (LatA), n=68 (CK666), n=28 (SMIFH2) shaft associated patches in 24, 17, 12, 6 dendrites of 16, 15, 10, 6 cells in 2 independent cultures.*

D. Quantification of normalized actin patch intensity as in **C**. Normalized actin patch intensity for spine associated patches was reduced in LatA (5 µM for 30 min) and SMIFH2 (30 µM for 90 min) treated groups. For shaft associated patches it was only reduced after LatA treatment. 1-way ANOVA with Dunnett's post hoc test. * p=0.03, *** p<0.001. *Same n as in C.*

E. Representative STED and confocal images of DIV18 primary hippocampal neurons treated with Brefeldin A (BFA, 100 ng/ml for 10 h), a drug that disrupts endosomes. Neurons were stained with α-MAP2 antibody and phalloidin-Atto647N, arrows indicate examples of actin patches. BFA treatment did not affect the number of actin patches, nor alter the effect of CK-666 (Arp2/3 inhibitor) and SMIFH2 (formin inhibitor) on actin patches. Scale bar: 5 µm.

Figure EV3 - Dendritic actin patches display high actin dynamics, but their existence and position are relative stable

A. Individual stills from time-lapse spinning-disk confocal imaging of a dendritic segment of a DIV16 hippocampal neuron, expressing eGFP and chromobody-tagRFP. Actin patches (arrows) are stable over the entire imaging period (60 min). Images are compensated for bleaching and drift corrected. The lookup table of individual channels is adjusted for representation. Scale bar: 10 µm.

B. Kymograph of the dendritic segment shown in **A**. The presence and position of actin patches is relative stable over a period of 60 min (arrows indicate examples of stable patches). Scale bar: 10 µm.

Figure EV4 - Characterization of PEX-GFP-KIF17 construct for controlled cargo-motor assay in living neurons

A. Western blot of cleared cortical lysate (input) and enriched microsome fraction stained with antibodies against myosin Va (myoVa), PMP70, PEX14 and β-actin shows enrichment of peroxisomal markers PMP70 and PEX14, and the presence of myosin V (myoVa) in the fraction.

B. Immuno-staining of peroxisomes enriched from rat brain, identified with the peroxisome markers PEX14 and PMP70, are negative for myosin V (myoV) and myosin VI (myoVI). Scale bar: 5 µm.

C. Upper panel: Schematic of a peroxisome coupled to constitutively active KIF17-VHH_{GFP} via PEX3-GFP. Both constructs are expressed on the same bicistronic P2A vector to ensure co-expression. Lower panel: representative kymographs from a time-lapse series of a DIV16 hippocampal neuron expressing PEX3-GFP (control; no motility) or PEX3-GFP-P2A-KIF17-$VHH_{GFP.}$ Bidirectional movement in dendrite and unidirectional movement (anterograde) in axon indicate the presence of KIF17 as the only processive microtubule-dependent motor. Scale bar: 2 µm, 10 s.

D, E. Analysis of the instant velocity and instant run lengths of KIF17-coupled peroxisomes moving in the anterograde or retrograde direction (corresponding to Figure **6E-J**). Peroxisomes transported by KIF17 move uniformly in both directions. 2-tailed unpaired Student's t-test. *n=14 (anterograde), n=17 (retrograde) of 17 dendritic segments of 5 cells in 1 culture.*

Figure EV5 - Effects of myosin V and myosin VI pharmacological inhibitors on LAMP1-eGFP motility

A. Representative kymographs from dendritic segments of a DIV16 primary hippocampal neuron expressing LAMP1-eGFP, before (control) and after treatment with the myosin V inhibitor MyoVin (30 µM, 30 min). Scale bar: 5 µm, 15 s.

B. Quantification of mobile and stationary lysosomes (LAMP1-eGFP). MyoVin treatment increased the number of stationary lysosomes, but did not significantly change the mobile fraction. 2-tailed paired Student's t-test. *** $p<0.001$. *n= 25 dendritic segments of 21 neurons in 3 independent cultures.*

C. Quantification of lysosome motility from kymographs as shown in **A**. Analyzed were the total time spent pausing (< 1 min), stationary (≥ 1 min), or moving in the anterograde or retrograde direction. MyoVin increased stationary time and reduced short-term pausing. RM-2-ANOVA with lysosome behavior and treatment as within group factors. $F(3, 72)=14.623$, $p<0.001$ with Newman-Keuls post hoc test ** p=0.001, *** p<0.001. *Same n as in B*

D. MyoVin treatment increased the cumulative peroxisome pausing time. Wilcoxon signed rank test. ** p=0.005. *Same n as in B.*

E. Cumulative frequency of the duration of pausing events of lysosomes (LAMP1-eGFP) in control (DMSO) and the presence of MyoVin. Fully stationary lysosomes were excluded. The presence of MyoVin did not change the pausing time distribution. 2-tailed Mann-Whitney U-test. *n=782 (control), n=654 (MyoVin) events in 25 dendritic segments of 21 cells in 3 independent culture.*

F. Analysis of the instant velocity (left) and instant run lengths (right) of lysosomes (LAMP1-eGFP) moving in the anterograde or retrograde direction. MyoVin treatment decreased instant velocities. Paired 2-tailed Student's t-test (mobile) or Wilcoxon matched paired (stationary) * p=0.012, ** p=0.0029. *Same n as in B.*

G. Representative kymographs from a dendritic segment of a DIV16 primary hippocampal neuron expressing LAMP1-eGFP, before (control) and after treatment with the myosin VI inhibitor TIP (4 µM, 30 min). Scale bar: 5 µm, 15 s.

H. Quantification of mobile and stationary lysosomes (LAMP1-eGFP). TIP has no significant effect on lysosome numbers. Paired 2-tailed Student's t-test (stationary) or Wilcoxon matched pairs test. *n= 22 dendritic segments of 19 cells in 3 independent cultures.*

I. Quantification of lysosome motility from kymographs as shown in **G**. Analyzed were the total time spent pausing (< 1 min), stationary (≥ 1 min), or moving in the anterograde or retrograde direction. Treatment with TIP slightly increased the long-term (≥ 1 min) stationary fraction. RM-2-ANOVA with lysosome behavior and treatment as within group factors. $F(3, 63)=3.46$, $p=0.021$ with Newman Keuls post hoc test. * p=0.01. *Same n as in H.*

J. TIP treatment did not significantly change the summed pausing time of lysosomes (LAMP1-eGFP). 1-sample t-test against 100 %. *Same n as in H.*

K. Cumulative frequency of the duration of pausing events of lysosomes (LAMP1-eGFP) in control (DMSO) and in the presence of TIP. Fully stationary lysosomes were excluded. TIP-treatment did not affect the distribution of pausing events. 2-tailed Mann-Whitney U-test. *n=1029 (control), n=908 (TIP) events of 22 dendritic segments of 19 cells in 3 independent cultures.*

L. Analysis of the instant velocity (left) and the instant run lengths (right) of lysosomes (LAMP1-eGFP) moving in the anterograde or retrograde direction. TIP treatment decreased the instant velocity and run length in both directions. 2-tailed Wilcoxon matched pairs test (anterograde velocity) *** p=0.0003 or paired 2-tailed Student's t-test * p=0.03 (anterograde run length) p=0.04 (retrograde run length), *** p< 0.001 (retrograde velocity). *Same n as in H.*

Figure 1

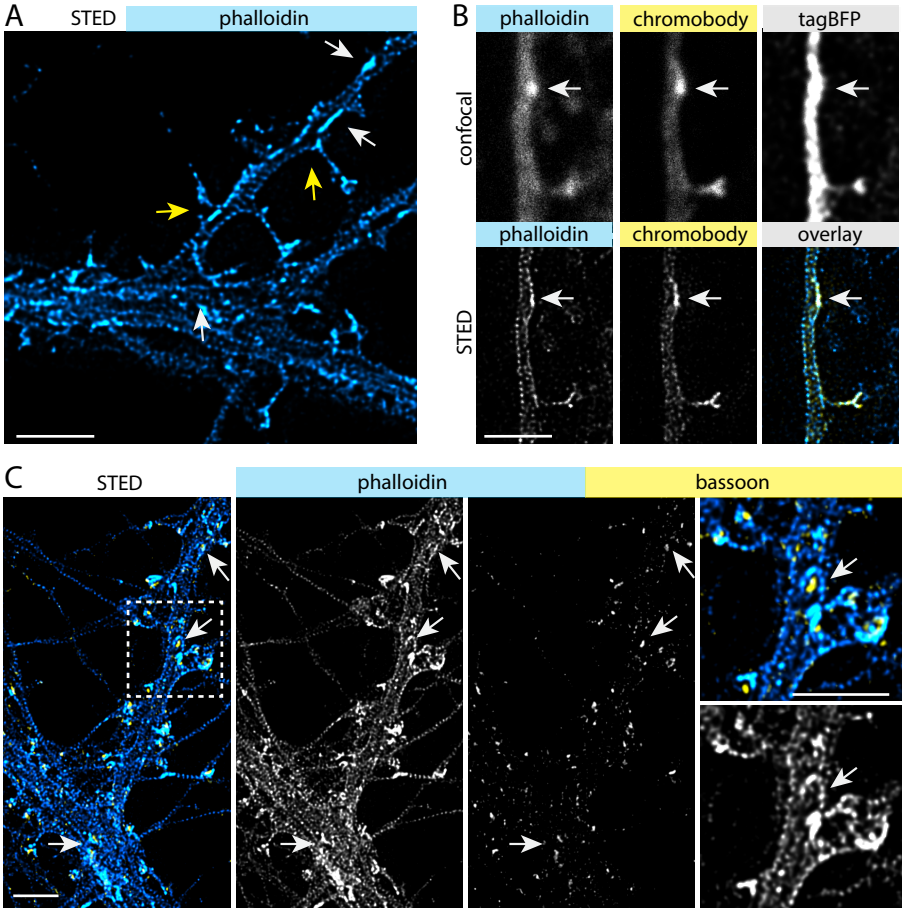

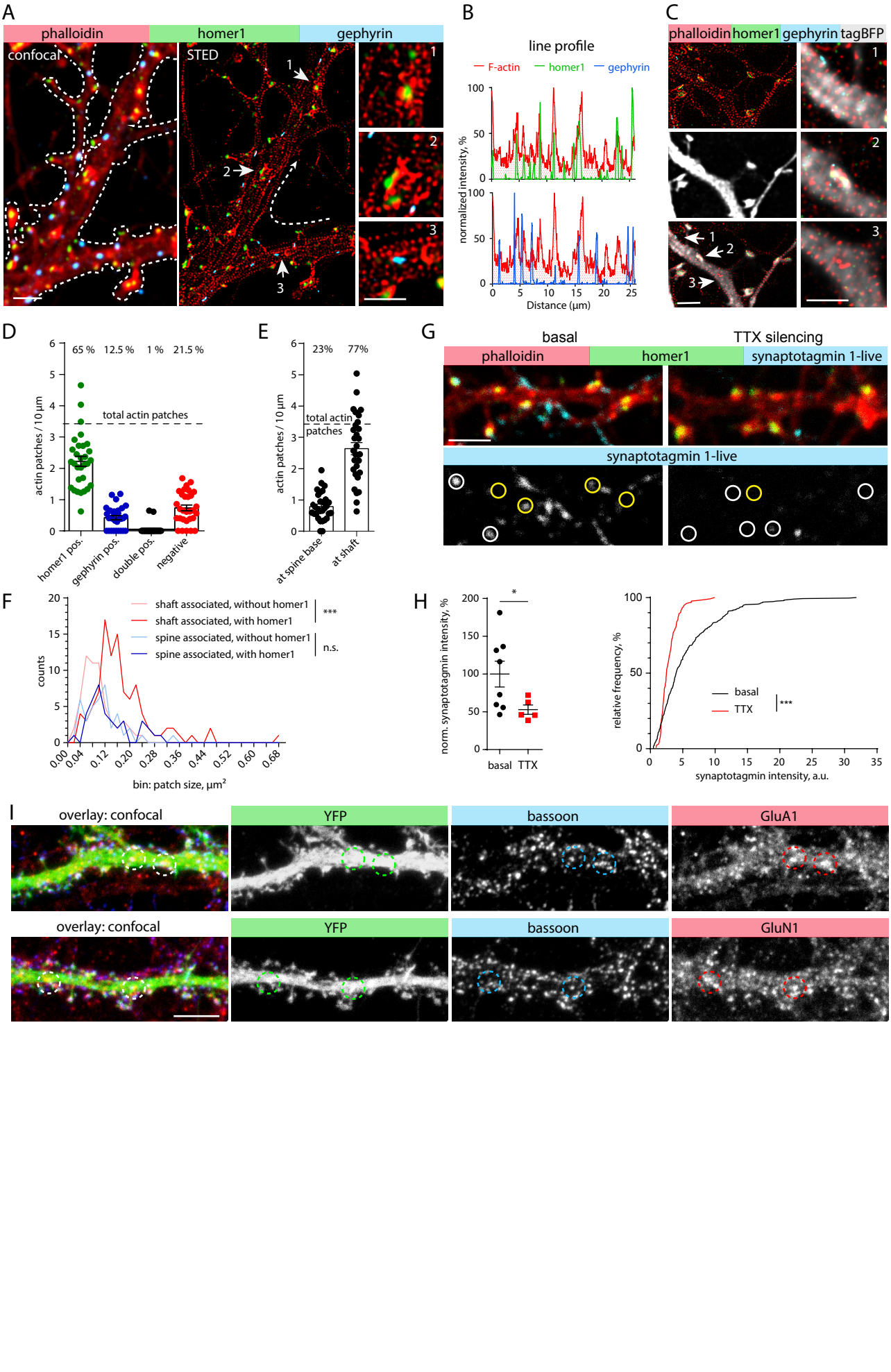

Figure 3

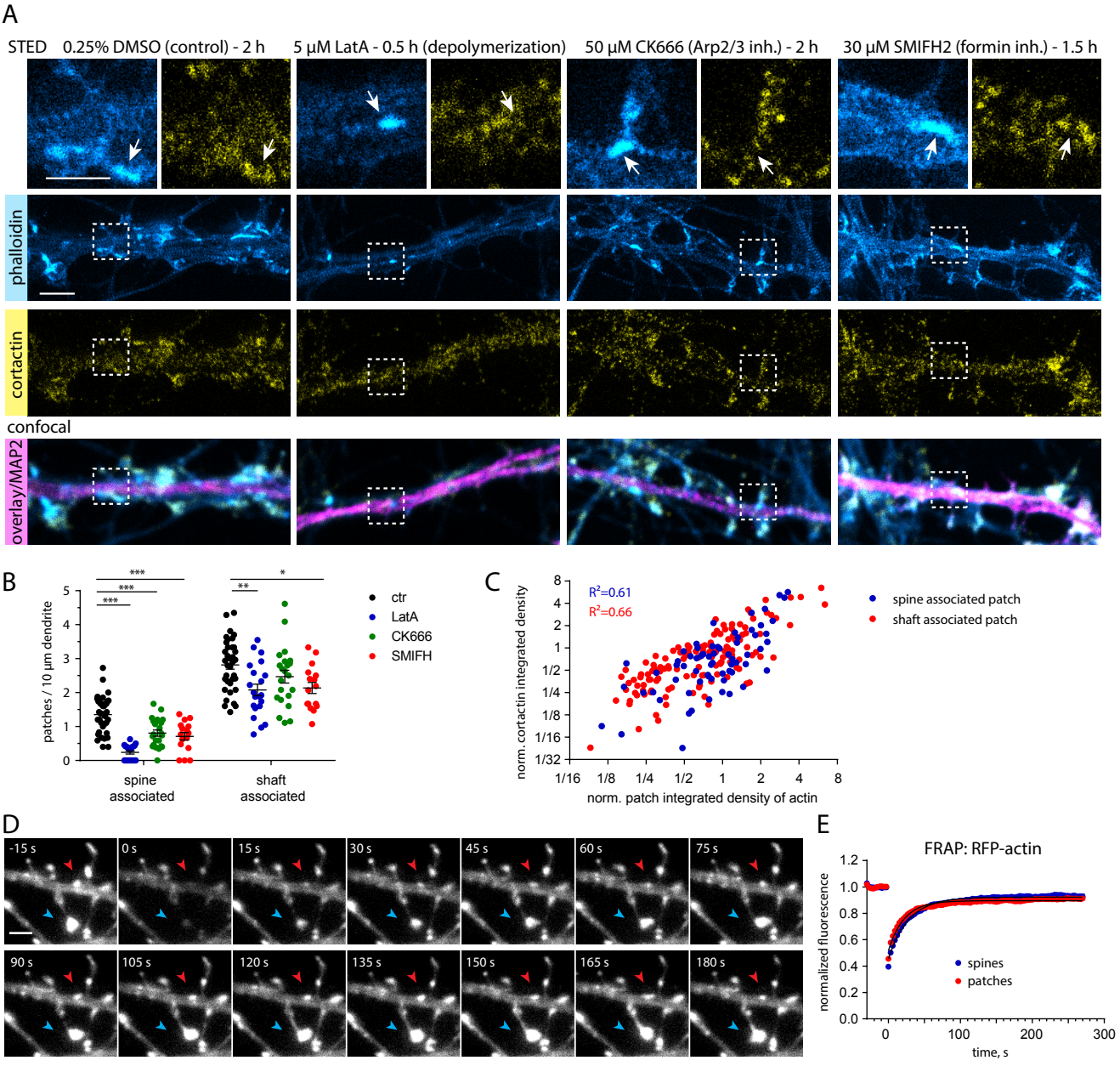

Figure 4

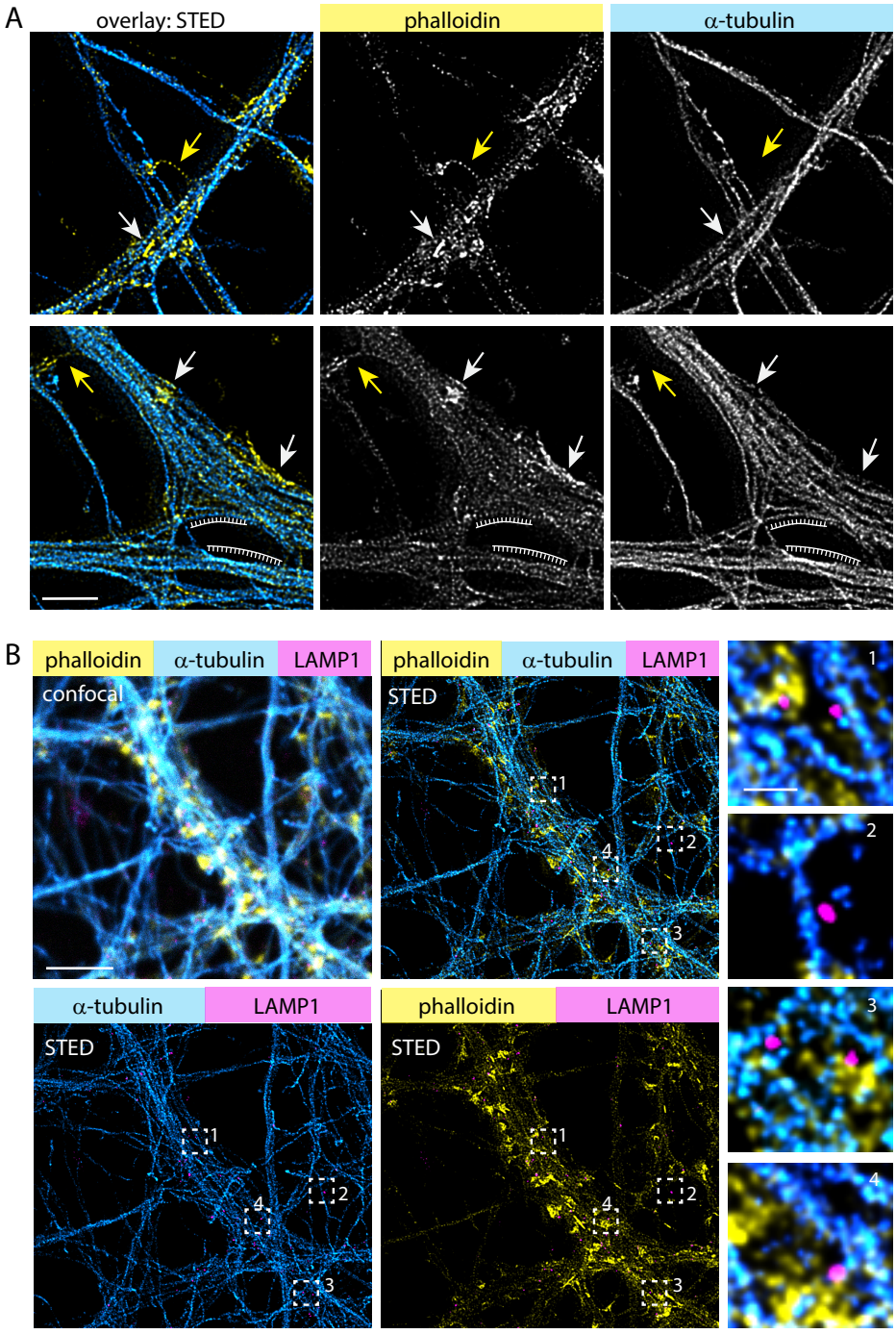

Figure 5

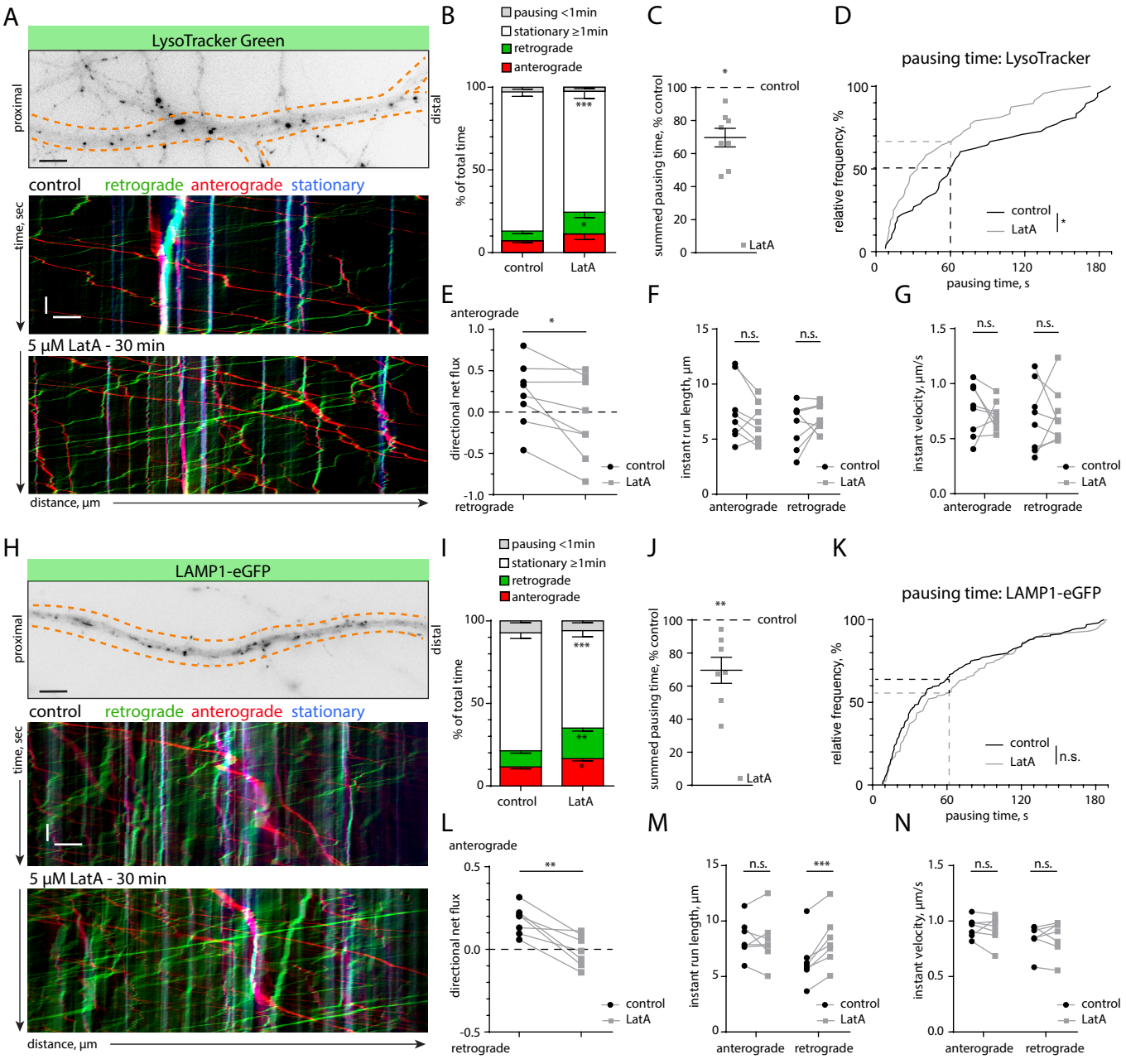

Figure 6

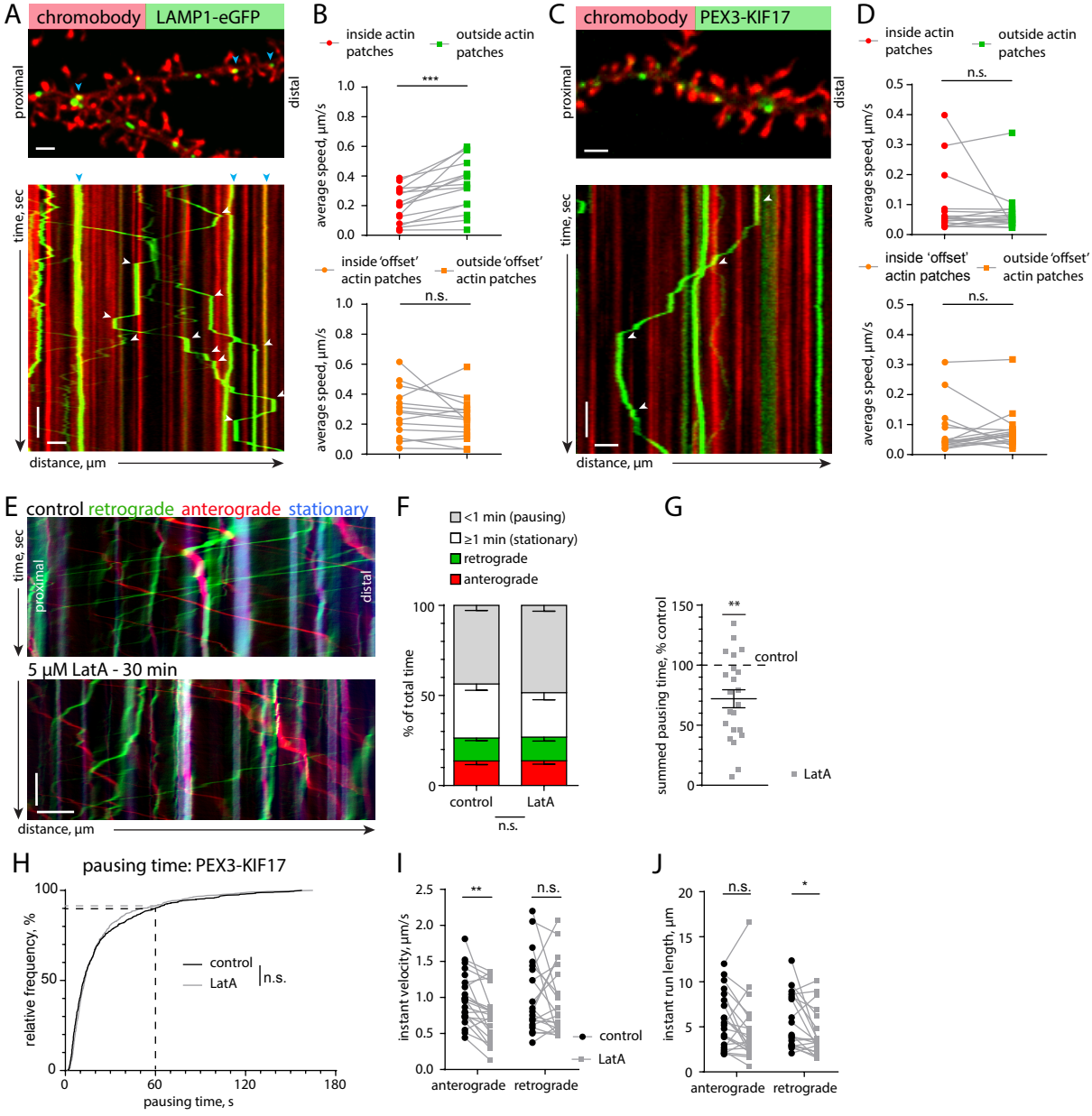

Figure 7